Materials Advances

ROYAL SOCIETY OF CHEMISTRY

PAPER

View Article Online
View Journal | View Issue

Cite this: *Mater. Adv.*, 2020, 1, 2467

Luminescence in external dopant-free scandium-phosphorus vanadate solid solution: a spectroscopic and theoretical investigation

Fengwen Kang, *[ab] Yongping Du,[cd] Philippe Boutinaud, [e] Guohuan Sun,[f] Xicheng Wang, [g] Jian Lu [b] and Sanshui Xiao *[a]

Spectrally tunable inorganic solid solutions discovered in the past few years generally cannot show spectral tuning properties without using either external rare earth (RE) (*e.g.*, Eu^{2+}, Ce^{3+}) and non-RE (*e.g.*, Mn^{2+}, Bi^{3+}) ions, or the coupling arrangement of these RE/non-RE ions as luminescent activator(s). Herein, we report a type of external dopant-free $Sc(P_x,V_{1-x})O_4$ ($0.0 \leq x \leq 1.0$) solid solution that exhibits color tuning, enhanced photoluminescence (PL) intensity, and improved thermally induced PL quenching stability. Our powder X-ray diffraction (XRD) and PL findings show that a gradual substitution of larger V^{5+} ions with smaller P^{5+} ions not only leads to the decrease of lattice parameters *a*(*b*)*c* and Sc–O bond lengths and the shrinkage of the cell volume (*V*), but also causes an initial redshift of the emission position from 495 nm to 524 nm as *x* increases to 0.2 followed by a subsequent blueshift back to 457 nm for $0.2 < x \leq 0.9$. Meanwhile, an enhancement of ~40% of room temperature emission intensity at $x = 0.3$, along with improved quantum efficiency (QE) and thermal PL quenching after adding an appropriate amount of P^{5+} ions, is observed in the $Sc(P_x,V_{1-x})O_4$ ($0.0 \leq x \leq 0.9$) solid solutions. Through a combined analysis and discussion of the density functional theory (DFT) and dielectric electronegativity calculations as well as the UV-vis diffuse reflectance and temperature-dependent PL spectral measurements, we reveal that the origin of this unusual yet regular spectral tuning and the improved PL properties mostly arises from the interplay of the bandgap energy adjustment, the bond covalency regulation, and the possible presence of a significant amount of oxygen vacancies, together with the closing structural rigidity caused by the lattice microenvironment modification. This work can provide insights into designing and discovering new external dopant-free inorganic solid solutions with color tunability, improved emission intensity and thermally induced PL quenching behavior, and allow gaining better understanding on how the key parameters govern the spectral tunability in virgin (or doped) zircon crystal systems at the same time.

Received 20th June 2020,
Accepted 8th September 2020

DOI: 10.1039/d0ma00438c

rsc.li/materials-advances

1. Introduction

Due to the merit of the flexible spectral wavelength selection for the device designer (*e.g.*, the phosphor-converted white LED designer), spectrally tunable inorganic solid solutions, formed by the modification of the host isostructural ions that feature the same valence yet different ion radii at the same coordination number (CN), are now receiving growing attention, but almost all of the previously reported solid solutions cannot exhibit their spectral tuning when they lack a rare-earth (RE) and non-RE ion (*e.g.*, Eu^{2+}, Ce^{3+}, Mn^{2+}, Bi^{3+} *etc.*) as the luminescent center, or the activators coupled by arrangement of these RE and/or non-RE ions.[1–7] Besides, some solid solutions, such as $(La,Gd)Sr_2AlO_5:Ce^{3+}$,[1] $Ca_{1-x}Li_xAl_{1-x}Si_{1+x}N_3:Eu^{2+}$,[2] $La_2Mg_{(1-w)}Zn_wTiO_6:Bi^{3+},Mn^{4+}$,[4] and $(Ca_{1-x}Sr_x)_{16}Si_{17}N_{34}:Eu^{2+}$,[6] are found to show unexpected photoluminescence (PL) properties, which include, for instance, the

[a] *DTU Fotonik, Department of Photonics Engineering, Technical University of Denmark, Lyngby, Denmark. E-mail: kangfengwen0597@126.com, saxi@fotonik.dtu.dk*
[b] *Department of Materials Science and Engineering, Department of Mechanical Engineering, City University of Hong Kong (CityU), 83 Tat Chee Avenue, Kowloon, Hong Kong, China*
[c] *Department of Physics, Technical University of Denmark, Lyngby, Denmark*
[d] *Department of Applied Physics and Institution of Energy and Microstructure, Nanjing University of Science and Technology, Nanjing 210094, Jiangsu, China*
[e] *Université Clermont Auvergne, SIGMA Clermont, Institut de Chimie de Clermont-Ferrand, 63000 Clermont-Ferrand, France*
[f] *The State Key Laboratory of Experimental Hematology, SKLEH, Institute of Hematology, Chinese Academy of Medical Sciences, Tianjin 300020, China*
[g] *Key Laboratory for Special Function Materials and Structural Design of the Ministry of Education, National and Local Joint Engineering Laboratory for Optical Conversion Materials and Technology, School of Physical Science and Technology, Lanzhou University, Lanzhou 730000, China*

enhanced PL intensity and/or the improved thermally induced PL quenching stability. However, RE- and non-RE-free inorganic solid solutions, which exhibit spectral tuning, enhanced PL intensity, and improved thermal PL stability simultaneously, have still not been reported so far. Note that the luminescent activators mentioned here are those ions that do not belong to any type of cation that constitutes the crystal host itself.

$LnBO_4$ (Ln = trivalent lanthanide or Sc^{3+}; B = P^{5+}, V^{5+}, and Nb^{5+}) is a type of important crystal system in the big family of inorganic oxides and possesses advantages of excellent thermal, chemical and mechanical stability, and optical properties. Relying on the Ln and B cations and the coupled arrangement of Ln and B cations, $LnBO_4$ features various crystal systems, including zircon (*e.g.*, $ScVO_4$,[8] $ScPO_4$,[9] and YVO_4,[10–12]), monazite (*e.g.*, $LaPO_4$[13]), fergusonite (*e.g.*, $GdNbO_4$[14]), and wolframite (*e.g.*, $ScNbO_4$[15]). As a result, diverse $LnBO_4$-related applications, such as laser host materials,[16] high-pressure mercury lamps,[17] color-television tubes,[18] infrared light detectors,[19] photocatalysis,[20] and ultrasonic generators,[21] have been discovered. Among the $LnBO_4$ crystals, zircon-type $ScVO_4$ and $ScPO_4$ crystals are two host materials particularly desirable for single trivalent RE (*e.g.*, Eu^{3+}/Tb^{3+},[22–24] Dy^{3+},[23] Ce^{3+}/Er^{3+} [23,24]) and non-RE (*e.g.*, Bi^{3+} [26–28]) dopants, or multiple dopants coupled by these RE and non-RE ions (*e.g.*, Eu^{3+}–Tb^{3+}/Sm^{3+}/Tm^{3+},[22–24] Eu^{3+}–Bi^{3+} [29]). Accordingly, a variety of emission colors, such as green from Tb^{3+},[22] red from Eu^{3+},[23] blue from Tm^{3+},[27] and reddish/red from Sm^{3+} [24] or Bi^{3+},[28] along with tunable colors from a combination of these dopants' emissions,[22,27,30] can be achieved using the $ScVO_4$ and $ScPO_4$ hosts. The crystal structures of $ScBO_4$ (B = V, P), as shown in Fig. 1a, are relatively simple, containing only one type of Sc and B site coordinated respectively by eight and four oxygen atoms, but the Sc–O bonds have two different lengths.[26,31–33] Since $ScVO_4$ and $ScPO_4$ are all crystallized in a tetragonal space group of $I4_1/amd$ and the [ScO_8] and [BO_4] polyhedral structures share the same oxygen atoms and/or oxygen edges, the formation of the $Sc(P_x,V_{1-x})O_4$ ($0 \le x \le 1$) solid solutions becomes, therefore, possible. According to the ICSD files no. 78074 (*i.e.*, for $ScVO_4$) and no. 74483 (*i.e.*, for $ScPO_4$), we show the average V···O···Sc···O···V and P···O···Sc···O···P bond lengths, from which we can understand well the difference between the two isostructural crystals. Besides, in principle, since the number of Sc ions in the as-expected solid solutions is fixed, a regular change of the crystal lattice cell with the larger V^{5+} ions (*i.e.*, 0.495 Å at four oxygen coordination numbers (CN)) being gradually replaced by the smaller P^{5+} (*i.e.*, 0.31 Å at CN = 4)[34–36] can therefore be expected further. In this case, when taken into account the emission positions of bulk $ScVO_4$ (*i.e.*, 465 nm,[25,33] 20.7 × 10^3 cm^{-3} (blue-green)[32]) and $ScPO_4$ (*i.e.*, 430 nm (blue) under a moist atmosphere,[32] or ~210 nm (UV, 5.6–5.9 eV) under dry conditions[37,38]), varying the V/P ratios in the as-expected $Sc(P_x,V_{1-x})O_4$ solid solutions may lead to spectral tuning. Meanwhile, due to the lattice microenvironment modification that results from the radii matching between the V^{5+} and P^{5+} ions, there may exist some unexpected PL properties. Furthermore, several experimental and theoretical studies[39–45] have confirmed existence of the oxygen vacancies/defects in the $ScVO_4$ crystals by means of *e.g.*, reduction of a $ScVO_4$ precursor under an H_2/N_2 flow,[39] three-step liquid phase co-precipitation reaction,[40] and two-,[41] three-[42] and four-step[43] solid state reactions in air, and the vacancies/defects play a significant role in adjusting the mechanical, optical, and magnetic properties of the $ScVO_4$ crystals.[40,42] In this case, the substitution of V^{5+} ions with P^{5+} ions would affect the presence of the $ScVO_4$-related vacancies/defects, typically in V-rich intermediate solid solution compounds. In this perspective, we believe that the vacancies/defects are also important in discussing the PL observations that we cannot predict but deserve to be taken into account seriously. Unfortunately, all of the aspects we observed above are still not discussed or noticed in the previous studies, which are also the major motivation of why we carry out this work.

In this work, we have prepared and characterized structurally and spectroscopically external dopant-free scandium-phosphorus vanadate solid solutions, *i.e.*, $Sc(P_x,V_{1-x})O_4$ ($0.0 \le x \le 1.0$). We show that the PL properties of $ScP_xV_{1-x}O_4$ ($0.0 \le x \le 0.9$) are very peculiar since: (1) emission is observed at room temperature, which is not expected in zircon orthovanadates, and (2) the emission position is found to first switch to longer wavelengths as x increases up to 0.3 and then tune back to shorter wavelengths as x increases further. This unusual behavior is investigated in detail based on Rietveld XRD refinement, bandgap energies and environmental factor calculations based respectively upon density functional theory (DFT) and dielectric theory of electronegativity, as well as UV-vis diffuse reflectance and temperature-dependent PL spectral measurements. The origin of this anomaly can allow gaining better insight into the key parameters governing the spectral tunability of virgin (or doped) zircon crystal systems.

2. Experimental details

Based upon the nominal chemical composition of $Sc(P_x,V_{1-x})O_4$ ($0.0 \le x \le 1.0$, with an interval x value of 0.1), we ground the raw reagents of Sc_2O_3 (99.9%), $NH_4H_2PO_4$ (99.99%), and NH_4VO_3 (99.95%) in an agate mortar and then fired the mixtures at 1100 °C for 2 h in an alumina tube furnace under air atmosphere. After cooling down to room temperature, the products were ground again in the same agate mortar for the below-mentioned characterization.

The powder X-ray diffraction (XRD) patterns were collected from a Rigaku D/max-IIIA X-ray diffractometer using Cu Kα radiation (λ = 1.5405 Å, 1.2° min^{-1}) and a scanning rate of 1.2° min^{-1} in the 2θ range of 10–90°. To understand better the dependence relationship between the lattice structural variation and the P/V substitution ratio, we analyzed further the raw XRD data by using a FullProf Suite program. The excitation and emission spectra at room and high temperature were recorded on a Hitachi F-7000 spectrophotometer equipped with a 150 W xenon lamp as the excitation source. During the spectral collection, we kept the emission and excitation slits to 2.0 nm and 2.5 nm, respectively. The internal quantum efficiency (IQE) and external quantum efficiency (EQE) values were measured using a home-

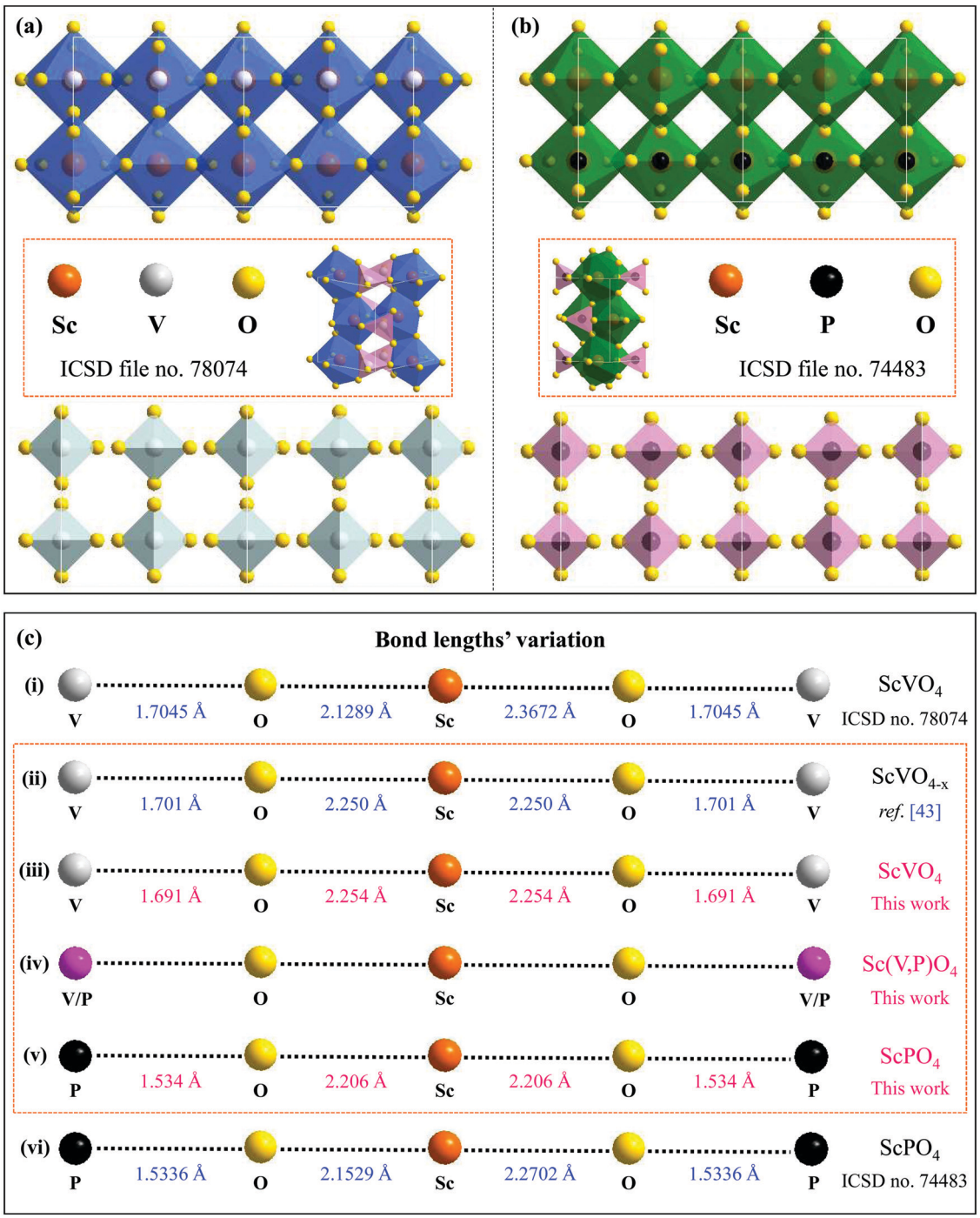

Fig. 1 (a and b) Double cell X [−1. . .+1] of the $ScVO_4$ and $ScPO_4$ isostructural crystals based on the ICSD file no. 78074 and no. 74483, respectively, from which we can clearly see the coordination environments of P^{5+} and Sc^{3+} cations and that the [ScO_8] and [PO_4] polyhedral structures share the same oxygen atoms or the same oxygen edges; (c) The Sc–O and V–O bond lengths of $ScPO_4$ and $ScVO_4$ based on the ICSD file no. 78074 (i) and no. 74483 (vi), as well as the average lengths of Sc–O and V–O bonds achieved from the $ScVO_{4-x}$ crystal (ii),[43] and the dependence of the average Sc–O and V/P–O bond length variation on the x value in the as-obtained $Sc(P_xV_{1-x})O_4$ ($0.0 \leq x \leq 1$) solid solutions (iii–v). Noted that the average interatomic Sc–O and V/P–O distances in (ii), (iii) and (v) were calculated using Vesta software and the atomic positions we used for establishing the model were based on the refined XRD atomic positions. Since the Vesta modeling process does not consider other factors such as the XRD pattern backgrounds, scale factors, and peak shapes, the calculated Sc–O and V/P–O distances are a little shorter than that derived from the refined data, but they are all correct and fine results.

built PL quantum yield (QY) collection system which used a 266 nm UV laser (Jewel Laser series) as the excitation source and equipped with an integrating sphere connected to an optical spectrometer. The UV-vis diffuse reflectance spectra of the solid solutions were recorded on a Hitachi U-4100 UV-vis-NIR spectrophotometer by using $BaSO_4$ as a reference.

3. Theoretical details

Our first-principle calculations were performed within the framework of DFT using the Vienna *ab initio* simulation package (VASP).[46] A kinetic energy cutoff of 400 eV was used for the plane wave basis set expansion and $2\pi \times 0.1$ Å^{-1} *k*-spacing had been chosen to sample the Brillouin zone. Lattice dynamical properties were calculated with projector-augmented plane-wave (PAW) potentials[47] with the generalized gradient approximation (GGA) of Perdew–Burke–Ernzerhof (PBE) parametrization.[48] The total energy and forces were converged to smaller than 10^{-7} eV and 10^{-2} eV Å^{-1} during the structural relaxation. To obtain an accurate bandgap, we also used the Heyd–Scuseria–Ernzerhof (HSE)[49] screened hybrid functional. We adopted virtual crystal approximation (VCA) to describe the V–P alloying.

A convenient manner to obtain information on the degree of covalency of a chemical bond in a crystal lattice is through calculating the environmental factor he(X) experienced by a cation site X of interest. The methodology derived from the dielectric theory of electronegativity[50–52] that had been applied successfully to a wide variety of physical problems in the years 60–70 before being extended to phosphors at the end of the 90's[53–56] and more recently in ref. 57. Following these models, we have the formula:

$$\mathrm{he}_{\mathrm{CN}}(\mathrm{X}) = \sqrt{\sum_{1}^{\mathrm{CN}} f_{c_{(\mathrm{X-L})}} \alpha_{(\mathrm{X-L})} Q_{\mathrm{L}}{}^{2'}}$$

where CN is the coordination number of the cation; X, L represent ligands (*i.e.*, oxygen in our case); $fc_{(\mathrm{X-L})}$ and $\alpha_{(\mathrm{X-L})}$ represent respectively the fractional covalency and the volume polarization of each individual chemical bond separating cation X from its nearby ligands L in binary units of type X_mL_n to which the initial host lattice must first be decomposed; Q_L is the effective charge carried by ligand L in each given X_mL_n unit. Q_L is calculated as $(n/m)\cdot Q_X$, where Q_X is the effective charge of cation X. This charge was taken as the bond valence sum of atom X in its polyhedron as calculated using the facilities provided in VESTA software.[58] The necessary values of the bond valence parameters were obtained from ref. 59 *i.e.*, 1.849 for Sc^{3+}, 1.803 for V^{5+} and 1.604 for P^{5+}. The procedure for decomposing a crystal system and calculating the sum of individual chemical bonds was described in detail in ref. 53, 54 and 57. Accordingly, the $ScVO_4$ crystal was decomposed into Sc(1/8)–O(8/3) + V–O(4/3), and the $ScPO_4$ crystal was decomposed into Sc(1/8)–O(8/3) + P–O(4/3). All details relative to the calculation of he(X) can be found in ref. 54 and 57 and will not be reproduced here for the sake of brevity.

4. Results

4.1 Analysis of structural phase-purity

The XRD patterns of $Sc(P_x,V_{1-x})O_4$ ($0.0 \le x \le 1.0$) (Fig. 2a) confirm the successful formation of continuous solid solutions that are crystallized in the zircon-type structure with a space group of $I4_1/amd$. As expected, the substitution of larger V^{5+} ions with smaller P^{5+} ions causes the shift of the diffraction position to a higher angle (Fig. 2b), revealing the shrinkage of the crystal lattice cell. The d_{hkl} values corresponding to the plane spacing (020) reflection are compiled in Table 1 and Fig. 2c(i), which are evaluated by the Bragg equation of $2d \sin\theta = \lambda$ (where λ is the X-ray wavelength, and θ is the diffraction angle).[25,26] All the raw XRD data are refined further using the Rietveld refining method, and four typical refined XRD patterns are shown in Fig. 3, *i.e.*, the $Sc(P_x,V_{1-x})O_4$ (x = 0.2 (Fig. 3a), 0.4 (Fig. 3b), 0.7 (Fig. 3c), and 0.9 (Fig. 3d)). The refined lattice parameters $a(b)c$ and cell volumes (V) are compiled in Table 1, which, together with the refined finial reliability factors, reveal that our refined results are desirable. The P^{5+} content dependent lattice parameters $a(b)c$ and V values can be linearly fitted (Fig. 2c(ii–iv)), revealing the regular variation of the crystal structure as the V^{5+} ions are replaced by the P^{5+} ions. Based on our refined parameters, we have re-drawn the crystal structure (Fig. 1b). Obviously, it is the same as that of Fig. 1a. Moreover, with Fig. 1c, we can also know how the V···O···Sc···O···V, V/P···O···Sc···O···V/P and P···O···Sc···O···P bond lengths change in the $Sc(P_x,V_{1-x})O_4$ ($0.0 \le x \le 1.0$) solid solutions with a substitution of larger V^{5+} ions with smaller P^{5+} ions.

4.2 Density functional theory (DFT) calculations and reflectivity spectra

Fig. 4a shows the results of density of state (DOS) calculations for the energy region associated with the valence band (VB) and conduction band (CB) of $Sc(P_x,V_{1-x})O_4$ (x = 0.2, 0.4, 0.6, 0.8) solid solutions. For bulk $ScPO_4$, the top of the VB and the bottom of the CB mainly consist of the O(2p) states with non-bonding character and the Sc(3d) empty states. The incorporation of V atoms results in the formation of antibonding V(3d) states at the bottom of the CB. These V(3d) states are strongly mixed with the Sc(3d) states, and their contributions become readily prominent as the V amount increases. The P(3p) states only weakly contribute to the bottom of the CB and can be neglected. The DFT-optimized parameters $a(b)c$ and cell volumes (V) are listed in Table 1, the tendency of which is consistent with that of the Rietveld refined parameters. The electronic bandgap (E_g) energies of $Sc(P_x,V_{1-x})O_4$ ($0.0 \le x \le 1.0$) and the corresponding DOS position maxima for Sc(3d), V(3d), P(3p) and O(2p) states are given in eV in Tables 2 and 3, respectively.

Our first-principles calculations reveal that a gradual substitution of V^{5+} ions with P^{5+} ions leads to a gradual increase of E_g energies (Table 2). Typically, the tendency of the E_g energies experiences a relatively flat increase with a $P(x)$ content of less or equal to 0.2. But after that the E_g energy shows a fairly rapid growth as the $P(x)$ content increases further. Although two DFT methods (*i.e.*, PBE, and HSE06) have been adopted to calculate the E_g energies and the E_g values derived from the HSE06 functional (Fig. 4b, curve 2) are larger than those from the PBE functional (Fig. 4b, curve 1), the variation tendency of E_g is on the whole the same. Besides, the VCA simulation matches well the tendency reported in our previous work[26] that used supercells to simulate the V–P alloying. To understand better this variation relationship and the differences of E_g values

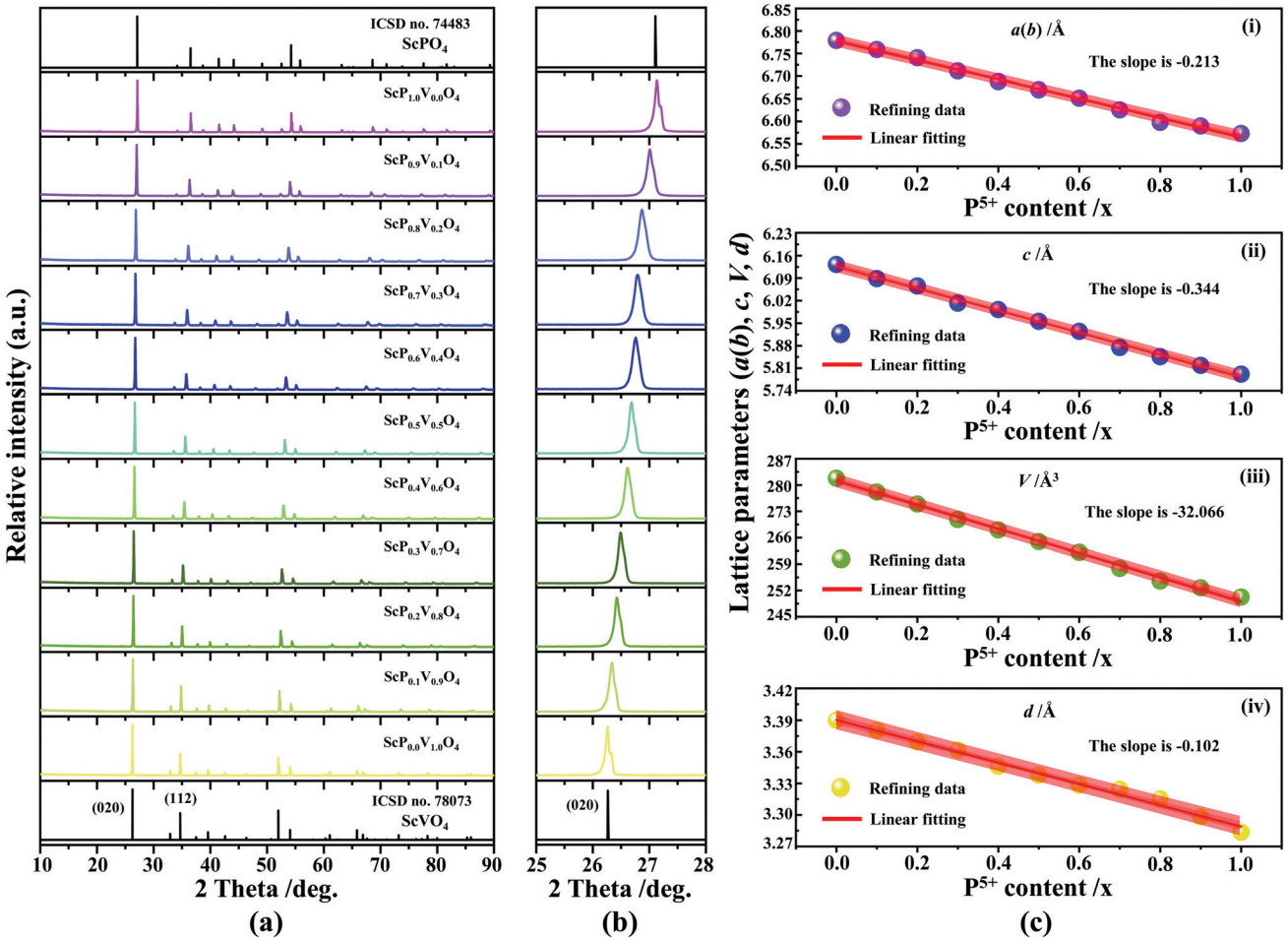

Fig. 2 (a) XRD patterns of the $Sc(P_xV_{1-x})O_4$ ($0.0 \leq x \leq 1$) solid solutions; (b) Enlarged XRD patterns within the range of 25–28°; (c) Experimentally calculated d_{hkl} values for the plane spacing (020) reflection (i), Rietveld refined lattice cell parameters $a(b)$ (ii), c (iii), and cell volume (V) (iv) of the as-obtained solid solutions as a function of P^{5+} (x) content.

Table 1 Rietveld refined parameters $a(b)c$ and cell volumes (V), and final reliability factors of $Sc(P_xV_{1-x})O_4$ ($0.0 \leq x \leq 1$) solid solutions, where the standard data, referenced from ICSD file no. 78073 (for $ScVO_4$) and file no. 74483 (for $ScPO_4$), are also incorporated. Meanwhile, the d_{hkl} values for the plane (020) reflection, the refined average Sc–O bond lengths and the corresponding covalence f_c of Sc–O bonds, as well as the DFT-optimized parameters $a(b)$ and c, have been also incorporated in this table

	Rietveld refined XRD parameters												DFT-Optimized $a(b)$ and c values	
X	$a(b)$/Å	c/Å	V/Å^3	R_p[a]/%	R_{wp}[b]/%	R_{exp}[c]/%	R_{Bragg}[d]/%	R_F[e]/%	Chi2	(020)/°	d_{hkl}/Å	Sc–O/Å	$a(b)$/Å	c/Å
No. 78073	6.78041	6.13451	282.03	—[f]	—	—	—	—	—	—	—	—	6.81615	6.14763
0.0	6.77894	6.13225	281.80	19.6	13.3	11.63	3.279	2.764	1.41	26.265	3.3901	2.3027	6.80319	6.11607
0.1	6.75879	6.08848	278.13	19.5	12.8	12.49	2.798	2.503	1.37	26.343	3.3803	2.2932	6.79330	6.07653
0.2	6.74064	6.06569	274.95	20.9	13.1	19.73	2.833	2.691	1.92	26.430	3.3693	2.2836	6.78678	6.05859
0.3	6.71137	6.01219	270.80	20.1	14.9	13.03	2.814	2.781	1.63	26.492	3.3616	2.2735	6.78060	6.03465
0.4	6.68809	5.99231	268.04	19.6	14.4	11.72	3.952	3.887	1.51	26.615	3.3463	2.2635	6.76314	5.99310
0.5	6.66973	5.95567	264.94	15.4	16.2	11.80	3.234	1.973	1.79	26.685	3.3377	2.2551	6.74104	5.94191
0.6	6.65137	5.92461	262.11	17.0	14.8	10.39	3.015	2.161	1.68	26.762	3.3283	2.2465	6.71116	5.88822
0.7	6.62547	5.87436	257.87	16.2	14.9	10.89	3.197	1.678	1.59	26.794	3.3244	2.2356	6.66779	5.83943
0.8	6.59784	5.84598	254.48	16.7	13.6	10.87	2.917	1.459	1.57	26.869	3.3153	2.2247	6.64385	5.81420
0.9	6.58996	5.81881	252.70	13.9	12.1	11.36	1.989	1.580	1.54	27.011	3.2982	2.2177	6.62343	5.78482
1.0	6.57320	5.79160	250.24	13.2	11.6	10.08	2.697	1.946	1.48	27.135	3.2834	2.2106	6.58242	5.76767
Nno. 74483	6.57872	5.79632	250.86	—	—	—	—	—	—	—	—	—	6.62504	5.81775

[a] R_p: profile factor. [b] R_{wp}: weighted profile. [c] R_{exp}: factor expected weighted profile factor. [d] R_{Bragg}: Bragg factor. [e] R_F: crystallographic factor. [f] —: not given.

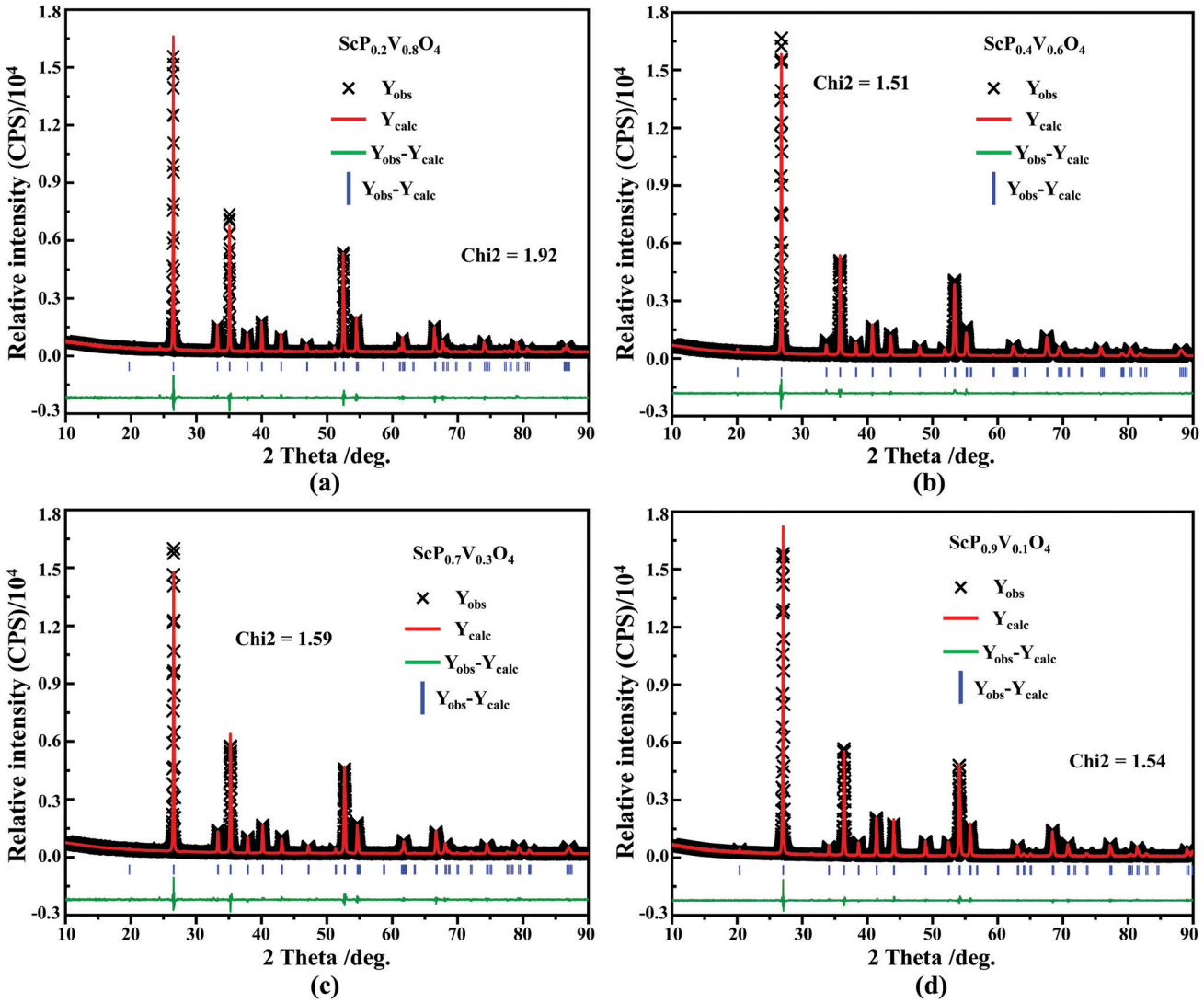

Fig. 3 Refined XRD patterns (–) of the typical samples of $ScP_{0.2}V_{0.8}O_4$ (a), $ScP_{0.4}V_{0.6}O_4$ (b), $ScP_{0.7}V_{0.3}O_4$ (c), and $ScP_{0.9}V_{0.1}O_4$ (d), where the Rietveld refining results (×), Bragg reflections (|) and the profile difference between observed and calculated values (–) are also given.

achieved by different DFT calculations, we show in Fig. 4b all the E_g energies.

In addition to the above DFT calculations, we also recorded the UV-vis diffuse reflectance spectra of $Sc(P_x,V_{1-x})O_4$ ($0.0 \leq x \leq 1.0$) at room temperature, and treated them using the Kubelka–Munk method through which the absorption coefficient α is estimated from the reflectance coefficient R using $\alpha = (1 - R)^2/2R$,[7,60,61] as shown in Fig. 4c. Obviously, the samples with $0 \leq x \leq 0.5$ present the strongest absorption in the UV-NUV region, and some of them also exhibit a certain strong absorption in the visible region (*e.g.*, violet-blue), which contributes to color the powders' body in yellow. In comparison, the samples with $x > 0.5$ only show reduced absorption in the visible region and thus appear as white body powders.

The reflectivity spectra corresponding to samples with $0 \leq x \leq 0.5$ can be decomposed into a sum of 4 Gaussian curves, as representatively illustrated in the inset of Fig. 4c for $Sc(P_{0.2},V_{0.8})O_4$. The energy positions of the first three absorption bands (*i.e.*, Abs0, Abs1, and Abs2 in order of increasing energy) are listed in Table 2. The fourth component was found in average at 5.22 ± 0.15 eV. In the zircon-type vanadate system, the lower absorbing band Abs0 reveals the presence of defects associated with oxygen vacancies that form in concomitance with vanadium atoms in valence state +4 or +3 located in the V^{5+} or Y^{3+} crystal sites.[62–64] Following the methodology introduced in ref. 65, we can qualitatively access the defect amounts by calculating the intensity ratio R = Abs0/(Abs0 + Abs1 + Abs2). This was made possible here by integrating the area of the corresponding Gaussian curves obtained after spectral decomposition. The values listed in Table 2 demonstrate the presence of defects in all phosphovanadates, with the amount being smaller in the end member $ScVO_4$ of the solid solution.

Finally, indicative E_g values were determined by plotting the relationship of $\alpha(h\nu)^2 = A(h\nu - E_g)$ where α, A and $h\nu$ represent the Kubelka–Munk absorption, the absorption constant and the photon energy, respectively. The experimental E_g data (Table 2, and the curve 3 of Fig. 4b) follow the trends obtained

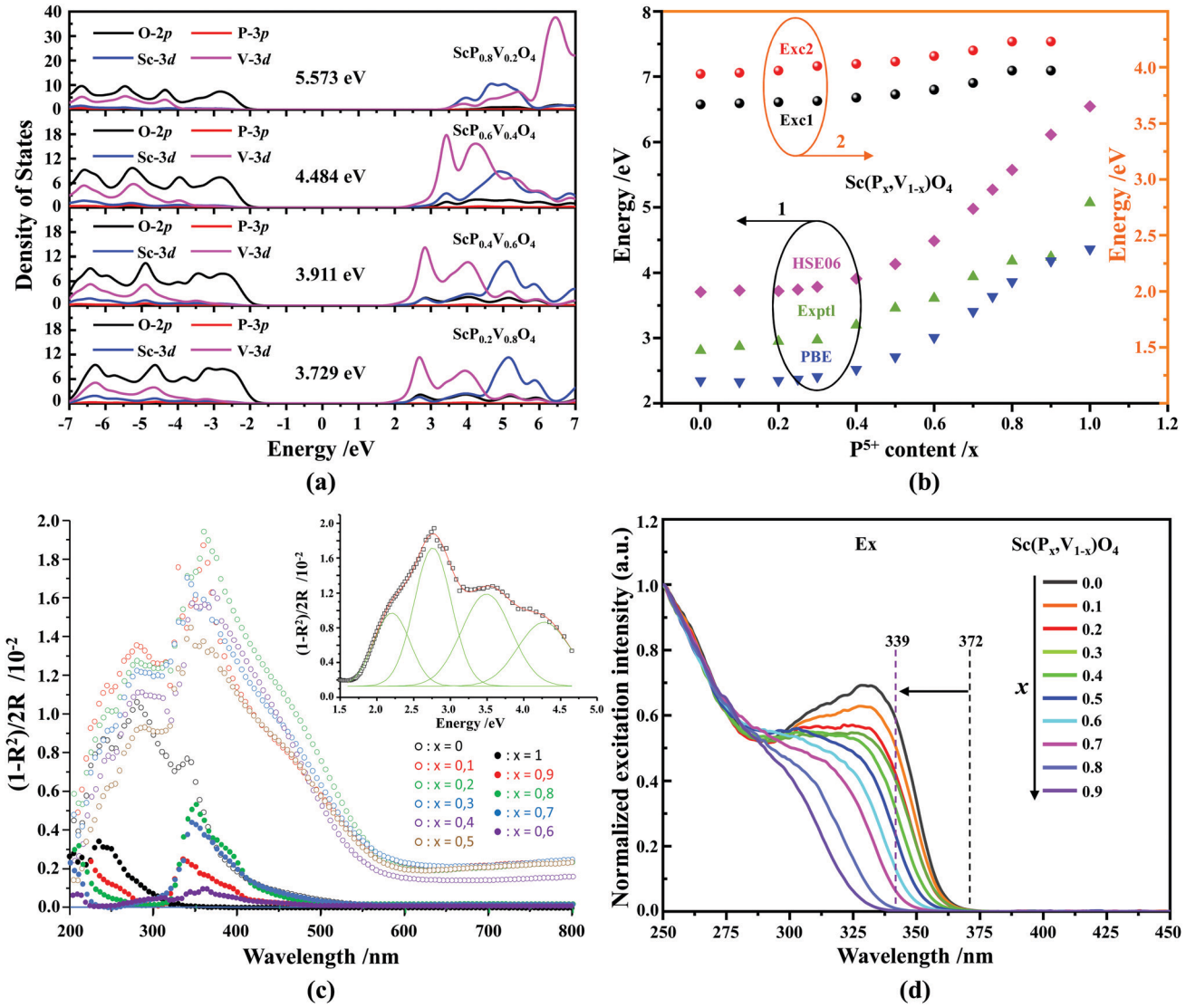

Fig. 4 (a) DFT-calculated DOS for the energy region in correspondence with the VB and CB of the $Sc(P_xV_{1-x})O_4$ (x = 0.2, 0.4, 0.6, 0.8) solid solutions; (b) Dependence of the P^{5+} (x) content on the PBE (blue), HSE06 (purple) and Kubelka–Munk (green) calculated E_g energies, as well as the decomposed Exc1 (black) and Exc2 (red) values; (c) UV-vis reflectivity spectra of $Sc(P_xV_{1-x})O_4$ (x = 0–1.0) solid solutions and a sum of 4 Gaussian decomposition for the $Sc(P_{0.2}V_{0.8})O_4$ sample (inset); (d) excitation spectra of the $Sc(P_xV_{1-x})O_4$ ($0.0 \leq x \leq 0.9$) solid solutions upon monitoring at the room temperature $(VO_4)^{3-}$ emission intensity maxima.

by theoretical calculations, despite the contribution of band Abs0 to the absorption edge.

4.3 Photoluminescence (PL) properties

According to the archival literature studies,[66,67] the structurally homogeneous zircon orthovanadates are not expected to show photoluminescence at room temperature. Following ref. 68, the excitation spectrum of the $(VO_4)^{3-}$ complex groups in $ScVO_4$ recorded at 77 K contains 3 distinct contributions in the spectral region that we have explored, *i.e.* Exc1 = 3.49 eV (355 nm), Exc2 = 3.90 eV (318 nm), and Exc3 beyond 5.14 eV (>240 nm), respectively. These excitation signals are due to $3t_2$ $(O^{2-}) \rightarrow 2e$ (V^{5+}) and t_1 $(O^{2-}) \rightarrow 2e$ (V^{5+}) electron transitions associated with O^{2-} (2p) $\rightarrow V^{5+}$ (3d) CT. The lowest excitation is ascribed to the $^1A_1 \rightarrow {}^1T_1$ transition; it corresponds to the bandgap of $ScVO_4$ and the excitation signal labelled as Exc1. The emission occurs from the close-lying $^3T_{1,2}$ triplets and has a charge transfer (CT) character.[66,69] It occurs at 483 nm (2.57 eV) in $ScVO_4$ at 77 K.[68] Here we observe that the $Sc(P_xV_{1-x})O_4$ ($x < 1$) solid solutions glow in the green–blue spectral region when excited by UV light at room temperature. Since the $ScPO_4$ does not glow and following earlier reports dedicated to YVO_4,[70–72] we ascribe this unusual room temperature emission to the tetrahedral tetroxo $(VO_4)^{3-}$ complex groups perturbed by the previously evidenced lattice defects. The excitation spectra collected in correspondence with this emission are shown in Fig. 4d. A band with increasing contribution as x is lowered appears in the near-UV region. We have successfully achieved the spectral decomposition of the low energy part of the excitation spectra shown in Fig. 4d (expressing in energy) into a sum of 3 Gaussian-shaped bands. The third, higher-lying, excitation band is positioned at 5.09 ± 0.04 eV (243 ± 2 nm) and is about 4 times broader (≈1.06 eV) compared

Table 2 Electronic band gap energies (E_g), absorption (*i.e.*, Abs0, Abs1, and Abs2) and excitation (*i.e.*, Exc1 and Exc2) values, emission peak positions (λ_{em}), relative emission intensity at room temperature (I_{emr}), CIE chromaticity coordinates, IQE and EQE values, as well as the thermal quenching temperatures ($T_{50\%}$), and activation energy (ΔE_a) of $Sc(P_x,V_{1-x})O_4$ ($0.0 \leq x \leq 1.0$) solid solutions. All energies are in eV

	Exptl E_g[a]		Calcd E_g[b]			Room temperature											High temperature	
x	Previous	Here	Previous	Here		Abs0	Abs1	Abs2	R/%	Exc1	Exc2	λ_{em}	I_{emr}/%	CIE	IQE/%	EQE/%	$T_{50\%}$/K	ΔE_a
—[c]	—	—	—	PBE	HSE06	—	—	—	—	—	—	—	—	—	—	—	—	—
0.0	2.80[&]	2.81	2.56[#]	2.344	3.706	3.27	3.63	4.29	12	3.67	3.94	2.50	100	(0.193, 0.240)	55.1	28.6	377.15	0.39
0.1	—	2.87	—	2.329	3.729	2.89	3.46	4.16	30	3.68	3.95	2.37	116.2	(0.212, 0.283)	57.3	28.3	405.15	0.43
0.2	—	2.95	—	2.348	3.721	2.73	3.42	4.33	21	3.69	3.97	2.36	131.4	(0.242, 0.365)	68.1	33.7	412.15	0.43
0.25	—	—	2.87 [#]	2.369	3.743	—	—	—	—	—	—	—	—	—	—	—	—	—
0.3	—	2.97	—	2.407	3.785	2.70	3.51	4.42	24	3.70	4.01	2.38	139.6	(0.253, 0.353)	66.7	42.3	444.15	0.48
0.4	—	3.20	—	2.520	3.911	2.89	3.46	4.33	27	3.73	4.03	2.42	136.2	(0.273, 0.373)	59.9	39.8	480.15	0.51
0.5	—	3.46	2.92 [#]	2.712	4.134	2.70	3.49	4.38	19	3.76	4.05	2.43	113.9	(0.277, 0.389)	50.1	36.5	457.15	0.50
0.6	—	3.61	—	3.008	4.484	2.97	3.49	4.13	18	3.80	4.1	2.51	74.6	(0.297, 0.402)	38.2	23.2	452.15	0.49
0.7	—	3.94	—	3.408	4.978	3.12	3.49	4.18	35	3.86	4.15	2.55	43.9	(0.303, 0.422)	35.3	10.4	438.15	0.49
0.75	—	—	3.20[#]	3.636	5.271	—	—	—	—	—	—	—	—	—	—	—	—	—
0.8	—	4.18	—	3.863	5.573	3.03	3.59	—	—	3.97	4.23	2.64	17.7	(0.273, 0.386)	28.0	5.40	431.15	0.48
0.9	—	4.24	—	4.182	6.114	2.76	3.42	—	—	3.97	4.23	2.71	13.1	(0.256, 0.350)	27.6	5.60	426.15	0.46
1.0	7.2[$]	5.07	4.11[#]	4.361	6.547	—	—	—	—	—	—	—	—	—	—	—	—	—

#, &, and $ denote the electronic bandgap (E_g) values are from ref. 13, 35 and 45, respectively. [a] Exptl: experimental. [b] Calcd: calculated. [c] —: Not given or measured.

Table 3 Position of DOS maxima for Sc(3d), V(3d), P(3p), and O(2p) states in the $Sc(P_x,V_{1-x})O_4$ ($0.0 \leq x \leq 1.0$) solid solutions

	DOS position maxima/eV			
x	Sc(3d)	V(3d)	P(3p)	O(2p)
0.0	5.16	2.67	—	−3.00
0.1	5.16	2.67	−4.51	−3.04
0.2	5.14	2.67	−4.59	−3.13
0.25	5.16	2.69	−4.66	−3.20
0.3	5.14	2.73	−4.70	−3.25
0.4	5.07	2.85	−4.87	−3.43
0.5	5.08	3.06	−5.11	−3.68
0.6	4.91	3.42	−5.38	−3.99
0.7	4.85	4.91	−5.39	−4.22
0.75	4.95	5.59	−5.27	−4.27
0.8	4.68	6.46	−5.48	−4.33
0.9	4.77	9.50	−7.22	−4.25
1.0	4.89	---	−7.80	−3.65

to the two other bands. The energy positions corresponding to Exc1 (curve 4) and Exc2 (curve 5) are plotted in Fig. 4b and compiled in Table 2. In the case of $ScVO_4$, the values deviate somehow from the values reported by Boulon,[68] which we ascribe to the perturbation (*i.e.*, the local distortion of the $(VO_4)^{3-}$ tetrahedral units) by lattice defects. Within the accuracy of the spectral decompositions, Exc1 and Exc2 agree with Abs1 and Abs2, respectively, while Abs3 agrees with Exc3. The agreement with DFT HSE06 calculations is also reasonably good for $x \leq 0.5$ and then shows a divergence. Interesting to note is that Exc1 is not the lower-lying absorption in the $Sc(P_x,V_{1-x})O_4$ system.

Despite the monotonic variation of the crystal structure and electronic properties of $Sc(P_x,V_{1-x})O_4$ as x increases from 0 to 1, we observe an irregular behavior of the $(VO_4)^{3-}$ emission excited at 260 nm (*i.e.*, corresponding to Abs2 or Exc2) that consists of a red shift of the position from 495 nm to 524 nm as x increases to 0.2 followed by a blue-shift back to 457 nm for $0.2 < x \leq 0.9$ (Fig. 5a–c). Concomitantly, we observe a continuous increase of the emission intensity with a maximum in the $Sc(P_{0.3},V_{0.7})O_4$ sample and then a rapid decrease of the emitted intensity as x is increased further (Fig. 5d). Moreover, it is shown in Table 2 and Fig. 5b (curve 2) that the variation tendency of EQE values under 266 nm laser excitation basically matches that of the relative emission intensity (Fig. 5d), and it is obvious that the $Sc(P_{0.3},V_{0.7})O_4$ sample has a maximum EQE of 42.3%. This PL behavior can be ascribed to the consequence of a complex compromise between the absorption rate at 260 nm (see Fig. 4c) and radiationless losses due to reabsorption by lattice defects contributing to band Abs0 and concentration quenching. In zircon vanadates, the concentration quenching involves the migration of the excitation energy among the isolated vanadate groups followed by radiationless losses of this excitation energy by energy transfer to sinks. As demonstrated by G. Blasse in the solid solution $Y(P,V)O_4$,[73] the energy migration and the related emission quenching by the concentration effect start operating for $(VO_4)^{3-}$ doping rates of $\approx$25%, which can be expected to explain the PL intensity variation of the $Sc(P,V)O_4$ in the same manner.

In addition to the room temperature spectra, we also have investigated the temperature-dependent emission spectra of $Sc(P_x,V_{1-x})O_4$ solid solution up to 300 °C, with the aim to collect information on the thermal quenching process and connect these data to the room temperature behaviors. We show the temperature-dependent emission spectra in Fig. 6a for the $ScP_{0.4}V_{0.6}O_4$ sample, which is taken as a representative of the thermal evolution of emission spectra and intensity for all other samples. We also show in Table 2 the temperature $T_{50\%}$ at which the emission intensity has lost 50% of its initial room temperature emission intensity in all compounds. The $T_{50\%}$ values, as exemplarily depicted by the fitted $T_{50\%}$ process of the $ScP_{0.4}V_{0.6}O_4$ sample (Fig. 6b), were obtained by using the integrated emission intensity through the Boltzmann sigmoidal equation:[74,75]

$$I(T) = \frac{A_1 - A_2}{1 + e^{(T-T_0)/dT}} + A_2$$

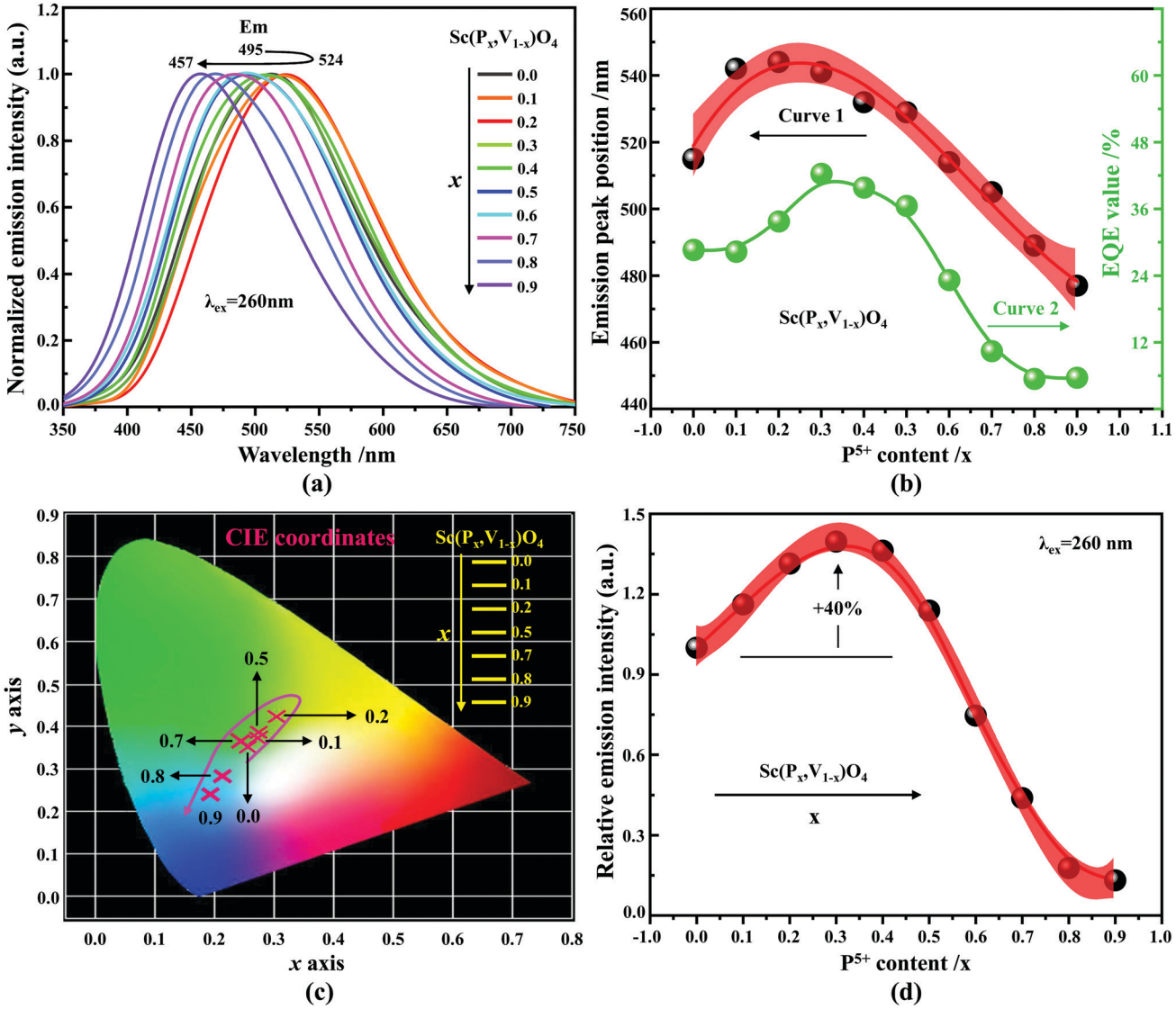

Fig. 5 (a) Normalized emission spectra of the $Sc(P_x,V_{1-x})O_4$ ($0.0 \leq x \leq 0.9$) solid solutions upon excitation at 260 nm; (b) emission peak position (curve 1) and external quantum efficiency (EQE) value (curve 2) against the P^{5+} (x) content; (c) CIE chromaticity coordinates of the $Sc(P_x,V_{1-x})O_4$ ($0.0 \leq x \leq 0.9$) solid solutions (note that the CIE values associated with the x values of 0.3, 0.4 and 0.6 are not shown, since they are close to other CIE values); (d) dependence of the P^{5+} (x) content on the room temperature emission intensity in the $Sc(P_x,V_{1-x})O_4$ ($0.0 \leq x \leq 0.9$) solid solutions.

where $I(T)$ is the emission intensity value at a given temperature; A_1 and A_2 are the initial value (left horizontal asymptote) and final value (right horizontal asymptote), respectively; T_0 and dT denote the center of the sigmoid and the change in T associated with the most significant change in $I(t)$ values, respectively; and T is the Kelvin temperature.

The temperature-dependent intensity variation of the $ScP_{0.4}V_{0.6}O_4$ sample was reproduced with a reliability above 99% using a single energy barrier model (Fig. 6c):[2,3,6,11,60,61,73–76]

$$\ln\left(\frac{I_0}{I_T} - 1\right) = -\frac{\Delta E_a}{kT}$$

where I_0 and I_T are the integrated emission intensity at room and higher temperatures, respectively; k is the Boltzmann constant; and ΔE_a is the energy separating the emitting and quenching states (*i.e.*, also referenced to as the activation energy). All ΔE_a values are also given in Table 2, and they follow the variation tendency analogous to the tendency of $T_{50\%}$ values (Fig. 6d), which jointly reveal that an appropriate amount of P content has improved the thermally induced PL quenching of the $Sc(P_x,V_{1-x})O_4$ solid solutions.

5. Discussion

As known from the archival literature,[77] the energy position of the O–V CT is related to the stabilization of the O^{2-} ions by the electric field created by the nearby cations; the smaller the radius and the higher the charge of these ions, the more stable the O^{2-} ions, the longer the O–V distance, the more ionic the character of the O–V bond, and the more the O–V CT moves to

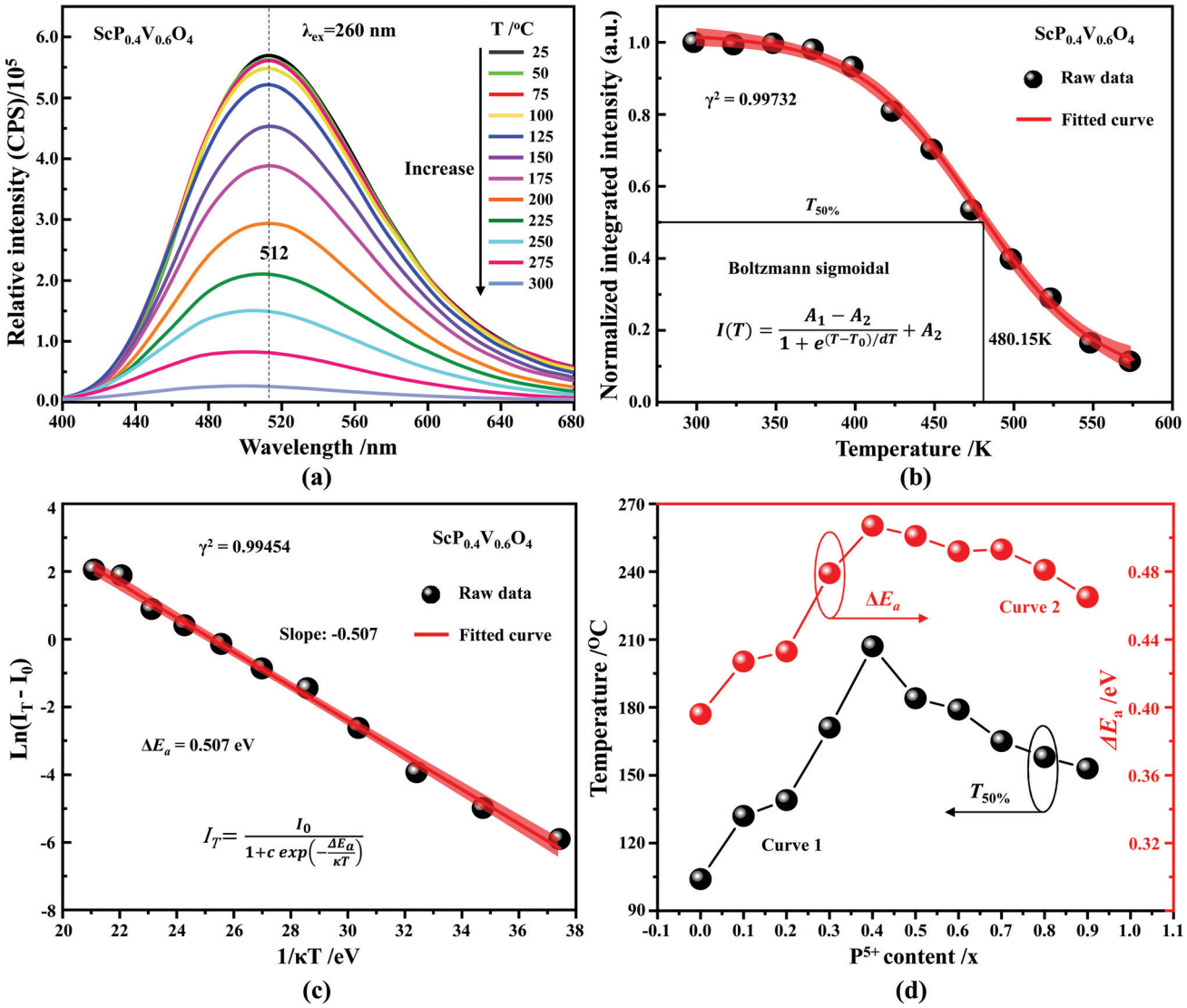

Fig. 6 (a) Temperature-dependent emission spectra (λ_{ex} = 260 nm) of the $ScP_{0.4}V_{0.6}O_4$ sample; (b) relative temperature-dependent integrated emission intensity of the $ScP_{0.4}V_{0.6}O_4$ and the fitting curve based on the Boltzmann sigmoidal equation; (c) fitted ΔE_a value for the thermal PL quenching of the $ScP_{0.4}V_{0.6}O_4$ sample; and (d) dependence of the P^{5+} (x) content on $T_{50\%}$ (curve 1) and ΔE_a (curve 2) values in the $Sc(P_xV_{1-x})O_4$ ($0.0 \leq x \leq 0.9$) solid solutions.

higher energy. Our results clearly demonstrate that this is what happens as x is increased in the $Sc(P_xV_{1-x})O_4$ solid solutions. We note, however, that the upward shift of the O–V CT is not regular; it is moderate up to $x \approx 0.5$ and then accelerates, which is referred to as the bandgap bowing. The lowering of the degree of covalency of the V–O bond on going from $ScVO_4$ to $ScPO_4$ is well confirmed by the regular increase of he(Sc) from 0.95 to 0.97 with a concomitant increase of the bond valence sum (BVS) of Sc from +2.81 to +3.07 that accounts for a reinforcement of the degree of covalency of the Sc–O bond at the expense of that of the V–O bond. In addition to these trends, the progressive increase of the phosphorous amount contributes to enhance the maximum phonon frequency of the crystal lattice (*viz.* with 914 cm^{-1} in $ScVO_4$[78] and up to 1083 cm^{-1} in $ScPO_4$[79]) and the lattice stiffness around the V atoms as formalized by calculating the lattice distortion $D(V)$ at V sites following the below equation:[3,60]

$$D = \frac{1}{n}\sum_{i=1}^{n}\frac{l_i - l_{av}}{l_{av}}$$

where l_i and l_{av} are the distances from V to the ith coordinated O atoms and the average V–O bond lengths, respectively. Values are plotted in Fig. 7a, where the decrease of $D(V)$ values with the increase of P^{5+} (x) content reveals a closing structural rigidity.

On the above grounds, we further discuss the evolution of the optical behavior of the $(VO_4)^{3-}$ groups going from isolated to concentrated systems. As specified earlier and represented in Fig. 7b, the emission intensity maxima of the $(VO_4)^{3-}$ groups experiences a redshift on going from $ScP_{0.9}V_{0.1}O_4$ to $ScP_{0.2}V_{0.8}O_4$

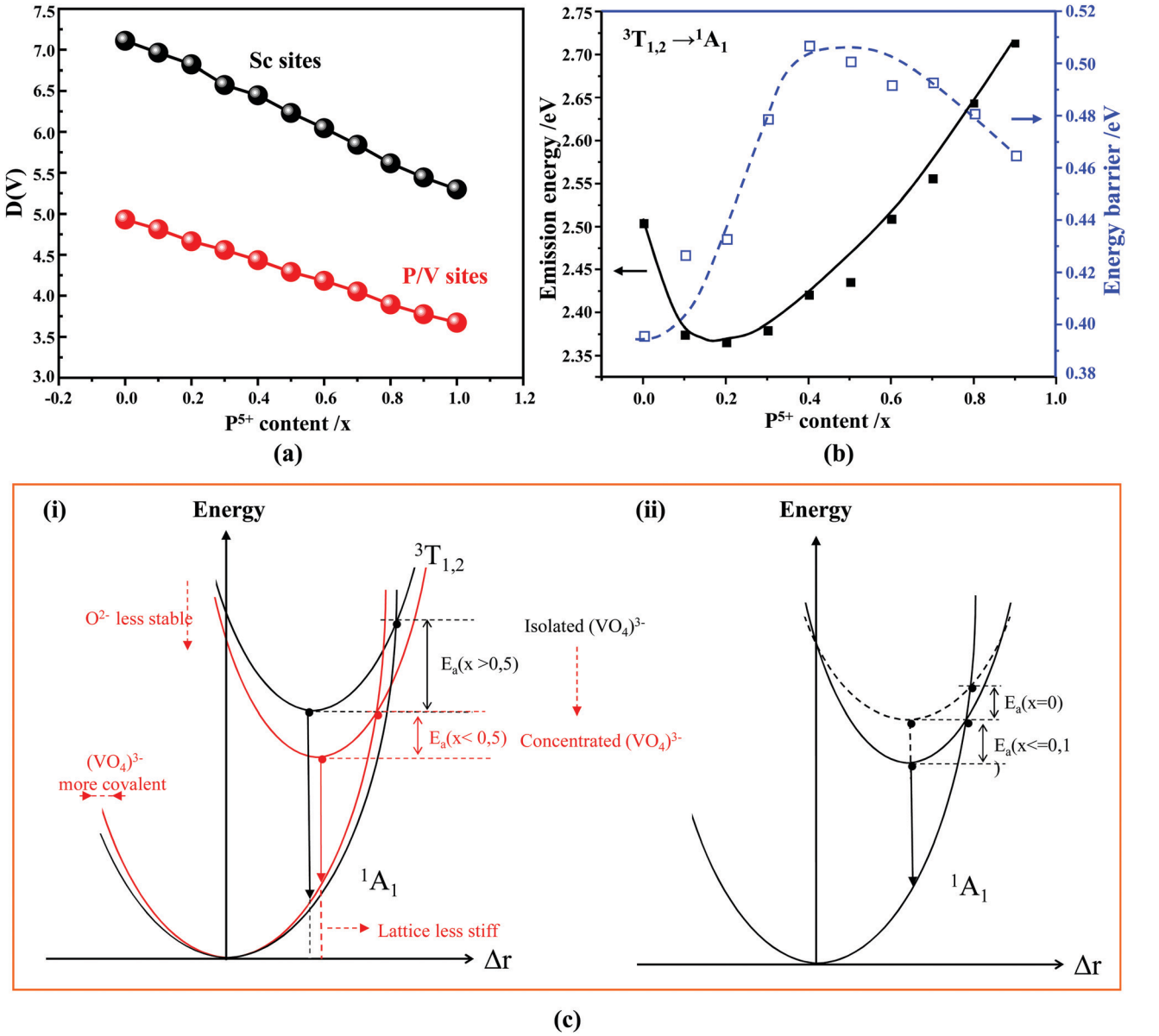

Fig. 7 (a) Calculated D values for the Sc (black) and P/V (red) sites; (b) variation of emission energy and energy barrier ΔE_a in the obtained $Sc(P_xV_{1-x})O_4$ solid solutions; (c) single coordinate configurational diagrams based on the potential energy of the $(VO_4)^{3-}$ luminescent unit.

followed by a sudden blueshift going from $ScP_{0.1}V_{0.9}O_4$ to $ScVO_4$. Concomitantly, the energy barrier ΔE_a associated with the thermal quenching of the emission first increases on going from $ScP_{0.9}V_{0.1}O_4$ to $ScP_{0.6}V_{0.4}O_4$ and then decreases regularly. These variations are due to the subtle consequences of the gradual changes experienced by the crystal lattice across the solid solutions. To conveniently and qualitatively understand these evolutions, we plot a single coordinate configurational diagram based on the potential energy of the $(VO_4)^{3-}$ luminescent unit (Fig. 7c(i)). In general, the average distance between the central metal ion and its surrounding anions is taken for this purpose. Within this model, the emission occurs from the thermalized close-lying $^3T_{1,2}$ excited states to the $^1A_1$ ground state after that internal radiationless relaxation from the absorbing $^1T_1$ state has occurred. Thermal quenching of the emission occurs by cross-over of $^3T_{1,2}$ to the $^1A_1$ ground state, and it depends critically on the equilibrium distance Δr of the ground and excited states. Thereby, we can understand that the decrease of the lattice stiffness as the vanadate amount is increased releases the constraints experienced by the V–O bond upon optical excitation, increases the Δr, and results in smaller values of ΔE_a and of the emission energy (Fig. 7c(i), from a black curve to a red $^3T_{1,2}$ curve). These effects are reinforced by the downward shift of the excited $^1T_1$ and $^3T_{1,2}$ states and by the lowering of the bonding force between the V and its nearby O atoms that results in a smaller force constant of the $^1A_1$ ground state potential curve (Fig. 7c(i), red $^1A_1$ curve) on going from $ScP_{0.9}V_{0.1}O_4$ to $ScP_{0.2}V_{0.8}O_4$. The observed blueshift of the $^3T_{1,2} \rightarrow {}^1A_1$ emission

Table 4 Average lengths of Sc–O and V/P–O bonds, bond valence sum (BVS) of Sc and V/P atoms, and environmental factor he(X) experienced by the Sc and V/P sites in the $ScVO_4$ and $ScPO_4$ crystals, where these data are extracted from and calculated basing on the archival literature (*i.e.*, $ScVO_{4-x}$),[43] a series of standard ICSD cards, and the end members of the as-obtained solid solutions (*i.e.*, $ScVO_4$ and $ScPO_4$)

Crystal lattice	Sc–O bond/Å	he(Sc)	BVS(Sc)	V/P–O bond/Å	he(V/P)	BVS(V/P)	Ref.
$ScVO_4$ – ICSD 78073	2.248	0.956	+2.86	1.704	3.316	+5.22	—
$ScVO_4$ – ICSD 164837	2.252	0.951	+2.81	1.693	3.350	+5.39	—
$ScVO_4$ – ICSD 169173	2.248	0.956	+2.86	1.709	3.307	+5.16	—
$ScVO_4$ – ICSD 174155	2.250	0.956	+2.85	1.701	3.323	+5.26	—
$ScVO_{4-x}$	2.250	0.956	+2.85	1.701	3.324	+5.26	43
$ScVO_4$	2.254	0.953	+2.81	1.691	3.354	+5.41	This work
$ScPO_4$ – ICSD 74483	2.211	0.967	+3.04	1.534	2.666	+4.84	—
$ScPO_4$ – ICSD 201132	2.207	0.966	+3.07	1.534	2.664	+4.83	—
$ScPO_4$ – ICSD 275305	2.208	0.967	+3.07	1.537	2.661	+4.80	—
$ScPO_4$	2.206	0.967	+3.07	1.534	2.666	+4.84	This work

in concomitance with the continuous decrease of ΔE_a on going from $ScP_{0.9}V_{0.1}O_4$ to $ScVO_4$ is accounted by a lowering of the force constant associated with the $^3T_{1,2}$ potential curve, as we show in Fig. 7c(ii) (from solid to dotted $^3T_{1,2}$ curve). We infer that this modification from the V–O bond is related to a smaller amount of oxygen vacancies in $ScVO_4$ as compared to $ScP_{0.9}V_{0.1}O_4$ (see Fig. 4c(i) and Table 2). In this regard, we show in Table 4 the environmental factors and bond valence sums that we have calculated for the end members of the solid solutions, including the data extracted from the archival literature studies and different ICSD files. Clearly, the results show little variability in the case of $ScPO_4$ but are more largely dispersed in $ScVO_4$. We estimate that this variability of BVS(V/P) and he(V/P) values is an indication of the amount of oxygen vacancies contained in the $ScVO_4$ lattice. To support this statement, the crystal structure of the vacancy contained $ScVO_4$ crystals, such as of $ScVO_{3.5+x}$[42] and $ScVO_{4-x}$,[43] has been investigated, where we observe that the presence of oxygen vacancies tends to increase the BVS(V) and correlated he(V) values. Our $ScVO_4$ compound and compound $ScVO_4$-ICSD 164837 exhibit larger BVS(V) and he(V) values of the series and are therefore suspected to contain the largest amount of oxygen vacancies. Furthermore, the BVS(P) and he(P) values of the $ScPO_4$ compound (*i.e.*, a compound with V-free oxygen vacancies) match precisely with the values calculated from other previously investigated $ScPO_4$ compounds. We are currently focusing on this particular point by investigating the *ESR* signatures of the $Sc(P_x,V_{1-x})O_4$ ($0.0 \leq x \leq 0.9$) solid solutions. This work is not presented here but under progress and will be the subject of a forthcoming paper soon.

6. Conclusion and perspectives

In summary, we used a conventional high temperature solid-state reaction method to synthesize a type of external dopant-free $Sc(P_x,V_{1-x})O_4$ ($0.0 \leq x \leq 1$) solid solution and reveal that they are all crystallized in the zircon-type structure with a space group of $I4_1/amd$ as confirmed by the powder XRD patterns and corresponding Rietveld refinement results. In addition, as expected, the XRD positions with the substitution of larger V^{5+} by smaller P^{5+} ions follow the Vegard's law nicely, where the shrinkage of the crystal lattice parameters $a(b)c$, cell volumes (V) and average Sc–O lengths is observed. Our PL findings show that beyond $ScPO_4$, other compounds, *i.e.*, $Sc(P_x,V_{1-x})O_4$ ($0.0 \leq x \leq 0.9$), exhibit that the emission position initially shifts from 495 nm to 524 nm followed by a subsequent blue-shift back to 457 nm as the x is gradually increased from 0.0 to 0.9. Meanwhile, an enhancement of ~40% of room temperature emission intensity, together with an optimal improved thermally induced PL quenching stability, referenced by the emission intensity of bulk $ScVO_4$, is observed in the intermediate $ScP_{0.3}V_{0.7}O_4$ and $ScP_{0.4}V_{0.6}O_4$ samples, respectively. The DFT calculations reveal the P^{5+} (x) content dependent electronic band-gap (E_g) energies in the $Sc(P_x,V_{1-x})O_4$ ($0.0 \leq x \leq 1.0$) solid solutions, and the variation tendency of the E_g values matches with those experimentally derived from the diffuse reflectance spectra. Through a combination of the DFT and dielectric electronegativity calculations and corresponding discussions, the underlying reason for the observed color tuning and the improved PL properties is mostly due to the interplay of the electronic bandgap energy adjustment, the bond covalency regulation, the gradual closing structural rigidity caused by the lattice microenvironment modification, and the contribution of lattice defects like oxygen vacancies. Based on the potential energy of the luminescent centre (*i.e.*, $(VO_4)^{3-}$ unit) and relevant analysis and discussion, a convenient yet qualitative single-coordinate configurational diagram is constructed further to discuss the observed PL evolutions.

Retrospecting this work, it is a little pity that the external dopant-free $Sc(P_x,V_{1-x})O_4$ ($0.0 \leq x \leq 1$) emission-tunable solid solutions do not belong to the class of phosphor materials particularly desirable for phosphor-converted white LEDs because of the following reasons: on one hand, the weakness of their excitation ranges less than the mainstream commercial UV LED chips with emission ranges of 375–410 nm and, on the other hand, their relatively low EQE (λ_{ex} = 266 nm laser, 5.6–42.3%) values compared to those of RE and/or non-RE doped phosphor materials such as $Sr_xBa_{2-x}SiO_4:Eu^{2+}$ (λ_{ex} = 405 nm laser, x = 43–73%, quantum yield (QY) = 88–90%),[2] $(Y,Lu)VO_4:0.02Bi^{3+}$ (λ_{ex} = 330 nm xenon lamp, EQE = 75% for $YVO_4:Bi^{3+}$, and 68% for $LuVO_4:Bi^{3+}$),[25] $ScVO_4:0.01Bi^{3+}$ (λ_{ex} = 330 nm, and 380 nm xenon lamp, EQE = 56%, and 57%, respectively),[28] $Ca_{0.97-x}Sr_xSc_2O_4:0.03Ce^{3+}$ (λ_{ex} = 437 nm xenon lamp, x = 0–1, internal QY (IQY) = 84.8–94.6%),[60] $K_2MgGeO_4:0.01Bi^{3+}$ (λ_{ex} = 335 nm xenon lamp, x = 0–1, EQE = 66.6%),[61] $Y_2Mo_4O_{15}:0.5\%Eu^{3+}$ (λ_{ex} = 465 nm xenon lamp, QY = 85%),[75] $SrYSi_4N_7:0.01Eu^{2+}$ (λ_{ex} = 365 nm xenon lamp, QE = ~41.6%),[76]

and $Sr_{2.975-x}Ce_{0.025}Ba_xAlO_4F$ (λ_{ex} = 405 nm InGaN LED, QE = ~100%),[80] as well as X2-type $Y_{1.98}SiO_5$:0.01Bi^{3+},0.01Eu^{3+} (λ_{ex} = 360 nm xenon lamp, EQE = 78%).[81] However, this situation is reasonable and can be understandable because the $Sc(P_x,V_{1-x})O_4$ solid solutions belong to the family of self-activated phosphors whose luminescence is mainly due to the existence of complex groups and/or defects.[82] As a result, in most cases, the self-activated phosphors usually can only show QE values less than 50%, such as those summarized by Dang *et al.*,[83] Huang *et al.*,[84] and Zhou *et al.*,[85] as well as $Ba_2V_2O_7$ (λ_{ex} = 360 nm xenon lamp, IQE = 47.5%),[86] $Ba_2V_2O_7$ (IQE = 25.0%),[87] $Mg_3V_2O_8$ (λ_{ex} = 350 nm xenon lamp, IQE = 6.0%),[88] $KCa_2Mg_2V_3O_{12}$ (λ_{ex} = 346 nm xenon lamp, IQE = 41.0%),[89] although a tiny of them are reported to have high IQE values, such as $Rb_3YV_2O_8$ (λ_{ex} = 362 nm xenon lamp, IQE = 71%),[83] and $Rb_3YV_2O_8$ (λ_{ex} = 362 nm xenon lamp, IQE = 82%),[83] and those summarized by Huang *et al.*,[84] and Zhou *et al.*[85] Looking into the IQE and/or EQE values we obtained, it is obvious that some of them, typically for the $Sc(P_{0.3},V_{0.7})O_4$ sample, are comparable to and can even be higher than those of many reported self-activated phosphors and some other RE/non-RE doped crystals, such as $ScVO_4$:0.02Bi^{3+} (λ_{ex} = 330 nm xenon lamp, EQE = 35%),[25] $CsPbCl_3$ (λ_{ex} = 360 nm xenon lamp, QY = 26.0 ± 0.3%),[90] $Cs_xK_{1-x}PbCl_3$:Eu^{3+} (λ_{ex} = 365 nm xenon lamp, EQE = 31.2%),[91] and $CsPbCl_3$:Mn^{2+} (λ_{ex} = 360 nm xenon lamp, QY = 27%).[92] Moreover, the improved thermal stability ($T_{50\%}$) of 480.15 K and/or activation energies (ΔE_a) of 0.51 eV for the $Sc(P_{0.4},V_{0.6})O_4$ solutions are also higher than or comparable to those of some RE/non-RE doped phosphors, for example, La_2MgTiO_6:0.005Bi^{3+} (λ_{ex} = 350 nm xenon lamp, $T_{50\%}$ = ~175 °C, ΔE_a = 0.27 eV),[4] La_2MgTiO_6:0.005Bi^{3+} (λ_{ex} = 410 nm xenon lamp, $T_{50\%}$ = ~250 °C, ΔE_a = 0.252 eV),[6] $CaSc_2O_4$:Ce^{3+} (λ_{ex} = 437 nm, $T_{50\%}$ = ~225 °C, ΔE_a = 0.195 eV),[60] K_2MgGeO_4:Bi^{3+} (λ_{ex} = 335 nm xenon lamp, ΔE_a = ~0.397 eV),[61] $Ca_{7.92}Mg_3Al_2Si_7O_{28}$:0.01$Eu^{2+}$ (λ_{ex} = 365 nm xenon lamp, ΔE_a = 0.2502 eV)[74] and $Y_{1.98}SiO_5$:0.01Bi^{3+},0.01Eu^{3+} (λ_{ex} = 360 nm xenon lamp, ΔE_a = 0.391 eV),[81] and the reported self-activated phosphors like $Rb_3YV_2O_8$ (λ_{ex} = 362 nm, $T_{50\%}$ = ~423 K, ΔE_a = ~0.264 eV),[83] $Ca_5Mg_4(VO_4)_6$ ($T_{50\%}$ = ~85 °C),[84] $KCa_2Mg_2V_3O_{12}$ (λ_{ex} = 346 nm, ΔE_a = 0.366 eV, $T_{50\%}$ = ~380 K),[89] $Na_{1.3}Mg_{1.7}V_{2.7}Mo_{0.3}O_{10}$ ($T_{50\%}$ = ~115 °C),[93] $Ca_2KZn_2(VO_4)_3$ (ΔE_a = 0.469 eV, $T_{50\%}$ = ~60 °C),[94] $CsVO_3$ (ΔE_a = 0.31 eV).[95]

More importantly, the fundamental aspects this work provided can deepen the understanding of the intrinsic working principle of the PL color tuning, enhanced PL intensity and improved thermal stability appeared in future spectrally tunable inorganic solid solutions. Meanwhile, it can provide some insights into designing and discovering new external dopant-free emission-tunable inorganic solid solutions through manipulating high valence secondary cations (*e.g.*, P^{5+} and V^{5+} cations).

Conflicts of interest

The authors declare that they have no known competing financial interests or personal relationships that could have appeared to influence the work reported in this paper.

Acknowledgements

We acknowledge the funding from the European Union's Seventh Framework Programme and Horizon 2020 Research and Innovation Programme under the Marie Sklodowska-Curie Actions grant agreement no. 609405 (FP7) and 713683 (H2020), Jiangsu Province Science Foundation for Youth (project no. BK20170821), and the National Science Foundation of China for Youth (project no. 11804160).

References

1 Z. Yu, Z. G. Xia, C. C. Su, R. L. Wang and Q. L. Liu, Effect of Gd/La substitution on the phase structures and luminescence properties of (La,Gd)Sr_2AlO_5:Ce^{3+} solid solution phosphors, *J. Mater. Chem. C*, 2015, **3**, 11629–11634.

2 A. D. Kristin, B. Jakoah, W. G. Michael, M. Alexander, P. Ralf, W. Holger, P. D. Steven and S. Ram, Consequences of Optimal Bond Valence on Structural Rigidity and Improved Luminescence Properties in $Sr_xBa_{2-x}SiO_4$:Eu^{2+} Orthosilicate Phosphors, *Chem. Mater.*, 2014, **26**, 2275–2282.

3 L. Wang, R. J. Xie, Y. Q. Li, X. J. Wang, C. G. Ma, D. Luo, T. Takeda, Y. T. Tsai, R. S. Liu and N. Hirosaki, $Ca_{1-x}Li_x$-$Al_{1-x}Si_{1+x}N_3$:Eu^{2+} solid solutions as broadband, color-tunable and thermally robust red phosphors for superior color rendition white light-emitting diodes, *Light: Sci. Appl.*, 2016, **5**, e16155.

4 G. C. Xing, Y. X. Feng, M. Pan, Y. Wei, G. G. Li, P. P. Dang, S. S. Liang, M. S. Molokeev, Z. Y. Cheng and J. Lin, Photoluminescence tuning in a novel Bi^{3+}/Mn^{4+} co-doped La_2A-TiO_6: (A = Mg, Zn) double perovskite structure: phase transition and energy transfer, *J. Mater. Chem. C*, 2018, **6**, 13136–13147.

5 Y. F. Liu, X. Zhang, Z. D. Hao, W. Lu, X. Y. Liu, X. J. Wang and J. H. Zhang, Crystal structure and luminescence properties of $(Ca_{2.94-x}Lu_xCe_{0.06})(Sc_{2-y}Mg_y)Si_3O_{12}$ phosphors for white LEDs with excellent colour rendering and high luminous efficiency, *J. Phys. D: Appl. Phys.*, 2011, **44**, 075402.

6 H. Chen, J. Y. Ding, X. Ding, X. C. Wang, Y. X. Cao, Z. Y. Zhao and Y. H. Wang, Synthesis, Crystal Structure, and Luminescence Properties of Tunable Red-Emitting Nitride Solid Solutions $(Ca_{1-x}Sr_x)_{16}Si_{17}N_{34}$:$Eu^{2+}$ for White LEDs, *Inorg. Chem.*, 2017, **56**, 10904–10913.

7 B. I. Won, G. Nathan, K. Joshua, B. Stuart, M. Alexander, H. Jerry, F. C. Bradley, P. D. Steve and S. Ram, Efficient and Color-Tunable Oxyfluoride Solid Solution Phosphors for Solid-State White Lighting, *Adv. Mater.*, 2011, **23**, 2300–2305.

8 W. Urban, EPR Parameters and Temperature Effects of Gd^{3+} in $ScVO_4$, *Phys. Status Solidi A*, 1970, **37**, 181–186.

9 F. X. Zhang, J. W. Wang, M. Lang, J. M. Zhang and R. C. Ewing, High-pressure phase transitions of $ScPO_4$ and YPO_4, *Phys. Rev. B: Condens. Matter Mater. Phys.*, 2009, **80**, 184114.

10 M. Yu, J. Lin and J. Fang, Silica Spheres Coated with YVO_4:Eu^{3+} Layers *via* Sol-Gel Process: A Simple Method To

Obtain Spherical Core-Shell Phosphors, *Chem. Mater.*, 2005, **17**, 1783–1791.

11 M. Yu, J. Lin, Z. Wang, J. Fu, S. Wang, H. J. Zhang and Y. C. Han, Fabrication, Patterning, and Optical Properties of Nanocrystalline YVO_4:A (A = Eu^{3+}, Dy^{3+}, Sm^{3+}, Er^{3+}) Phosphor Films *via* Sol–Gel Soft Lithography, *Chem. Mater.*, 2002, **14**, 2224–2231.

12 M. Yu, J. Lin and S. B. Wang, Effects of x and R^{3+} on the luminescent properties of Eu^{3+} in nanocrystalline $YV_xP_{1-x}O_4$:Eu^{3+} and RVO_4:Eu^{3+} thin-film phosphors, *Appl. Phys. A.*, 2005, **80**, 353–360.

13 T. S. Michael, L. M. Martha and E. D. M. Peter, Synthesis of monoclinic monazite, $LaPO_4$, by direct precipitation, *J. Mater. Chem.*, 2009, **19**, 5720–5722.

14 J. W. Hou, R. Zhou, J. W. Zhang, Z. P. Wang, Z. M. Zhang and Z. J. Ding, Pressure and Temperature Study on the Structural Stability of $GdNbO_4$:Eu^{3+}, *J. Phys. Chem. C*, 2017, **121**, 14787–14794.

15 G. Blasse, G. J. Dirksen and L. H. Brixner, The influence of structural disorder on the luminescence of niobates: scandium niobate ($ScNbO_4$) and magnesium niobate ($MgNb_2O_6$), *Mater. Chem. Phys.*, 1986, **14**, 485–494.

16 O. Guillot-Noel, B. Viana, B. Bellamy, D. Gourier, G. B. Zogo-Mboulou and S. Jandl, Spectroscopic evidence of inhomogeneous distribution of Nd^{3+} in YVO_4, YPO_4 and $YAsO_4$ crystals, *Opt. Mater.*, 2000, **13**, 427–437.

17 E. W. Herold, A History of Color Television Displays, *Proc. IEEE*, 1976, **64**, 1331–1338.

18 C. P. Frank and K. L. Albert, YVO_4:Eu: a Highly Efficient, Red-Emitting Phosphor for High Pressure Mercury Lamps, *Appl. Opt.*, 1966, **5**, 1467–1468.

19 L. C. Meng, L. HØgstedt, P. Tidemand-Lightenberg, C. Pedersen and P. J. Rodrigo, GHz-bandwidth upconversion detector using a unidirectional ring cavity to reduce multilongitudinal mode pump effects, *Opt. Mater. Express*, 2017, **25**, 14783–14794.

20 Y. Shiraishi, S. Takeshita and T. Isobe, Two Photoenergy Conversion Modes of YVO_4:Eu^{3+} Nanoparticles: Photoluminescence and Photocatalytic Activity, *J. Phys. Chem. C*, 2015, **119**, 13502–13508.

21 D. M. Li, P. F. Li, Y. Li, X. X. Wu, G. Y. Fu, Z. X. Liu, X. L. Wang, Q. L. Cui and H. Y. Zhu, High-Pressure Studies of Rubidium Azide by Raman and Infrared Spectroscopies, *J. Phys. Chem. C*, 2015, **119**, 16870–16878.

22 R. Y. Mi, J. Chen, Y. G. Liu, M. H. Fang, L. F. Mei, Z. G. Huang, B. C. Wang and C. L. Zhao, Luminescence and energy transfer of a color tunable phosphor: Tb^{3+} and Eu^{3+} co-doped $ScPO_4$, *RSC Adv.*, 2016, **6**, 28887–28894.

23 J. A. Dorman, J. H. Choi, G. Kuzmanich and J. P. Chang, High-Quality White Light Using Core-Shell RE^{3+}:$LaPO_4$ (RE = Eu, Tb, Dy, Ce) Phosphors, *J. Phys. Chem. C*, 2012, **116**(23), 12854–12860.

24 H. J. Chang, Y. S. Zhu, J. Xie, H. Y. Li, B. T. Liu, S. L. Xu, X. J. Xie, L. Huang and W. Huang, Surfactant effect on and luminescence tuning of lanthanide-doped $ScPO_4{\cdot}2H_2O$ microparticles, *J. Mater. Chem. C*, 2015, **3**, 12385–12389.

25 F. W. Kang, M. Y. Peng, X. B. Yang, G. P. Dong, G. C. Nie, W. J. Liang, S. H. Xu and J. R. Qiu, Broadly tuning Bi^{3+} emission via crystal field modulation in solid solution compounds (Y,Lu,Sc)VO_4:Bi for ultraviolet converted white LEDs, *J. Mater. Chem. C*, 2014, **2**, 6068–6076.

26 F. W. Kang, G. H. Sun, P. Boutnaud, F. Gao, Z. H. Wang, J. Lu, Y. Y. Li and S. S. Xiao, Tuning the Bi^{3+}-photoemission color over the entire visible region by manipulating secondary cations modulation in the $ScV_xP_{1-x}O_4$:Bi^{3+} ($0 \leq x \leq 1$) solid solution, *J. Mater. Chem. C*, 2019, **7**, 9865–9877.

27 D. Y. Shen, Y. F. Zhang, X. M. Zhang, Z. L. Wang, Y. F. Zhang, S. S. Hu and J. Yang, Morphology/phase controllable synthesis of monodisperse ScVO4 microcrystals and tunable multicolor luminescence properties in Sc(La)$VO_4(PO_4)$:Bi^{3+},Ln^{3+} phosphors, *CrystEngComm*, 2018, **20**, 5180–5190.

28 F. W. Kang, X. B. Yang, M. Y. Peng, L. Wondraczek, Z. J. Ma, Q. Y. Zhang and J. R. Qiu, Red Photoluminescence from Bi^{3+} and the Influence of the Oxygen-Vacancy Perturbation in $ScVO_4$: A Combined Experimental and Theoretical Study, *J. Phys. Chem. C*, 2014, **118**, 7515–7522.

29 F. F. Chi, Y. G. Qin, F. F. Hu, X. T. Wei, Y. H. Chen, C. K. Duan and M. Yin, Efficient red-emitting phosphor $ScVO_4$ doped with Bi^{3+} and Eu^{3+} for near-ultraviolet-activated solid-state lighting, *J. Mater. Sci.*, 2017, **52**, 11592–11597.

30 H. L. Xu, B. Xu, R. Liu, X. W. Li, S. Q. Zhang, C. Y. Ouyang and S. L. Zhong, Facile microwave synthesis of $ScPO_4{\cdot}2H_2O$ flowerlike superstructures: morphology control, electronic structure and multicolor tunable luminescent properties, *CrystEngComm*, 2017, **19**, 5787–5796.

31 W. O. MilliganD, D. F. Mullica, G. W. Beall and L. Boatner, Structural investigations of YPO_4, $ScPO_4$, and $LuPO_4$, *Inorg. Chim. Acta*, 1982, **60**, 39–43.

32 G. Blasse and A. Bril, Luminescence of Phosphors Based on Host Lattices ABO_4 (A is Sc, In; B is P, V, Nb), *J. Chem. Phys.*, 1969, **50**, 2974–2980.

33 F. W. Kang, H. S. Zhang, L. Wondraczek, X. B. Yang, Y. Zhang, D. Y. Lei and M. Y. Peng, Band-Gap Modulation in Single Bi^{3+}-Doped Yttrium-Scandium-Niobium Vanadates for Color Tuning over the Whole Visible Spectrum, *Chem. Mater.*, 2016, **28**, 2692–2703.

34 L. H. Ahrens, The use of ionization potentials Part 1. Ionic radii of the elements, *Geochim. Cosmochim. Acta*, 1952, **2**, 155–169.

35 L. Pauling, *The Nature of the Chemical Bond*, *Cornell University Press*, Ithaca, 1961.

36 R. D. Shannon, Revised Effective Ionic Radii and Systematic Studies of Interatomic Distances in Halides and Chalcogenides, *Acta Crystallogr., Sect. A: Cryst. Phys., Diffr., Theor. Gen. Crystallogr.*, 1976, **32**, 751.

37 A. N. Trukhin, K. Shmits, J. L. Jansons and A. B. Lynn, Ultraviolet luminescence of $ScPO_4$, $AlPO_4$ and $GaPO_4$ crystals, *J. Phys.: Condens. Matter*, 2013, **25**, 385502.

38 A. Trukhin and L. A. Boatner, Electronic Structure of ScPO4 Single Crystals: Optical and Photoelectric Properties, *Mater. Sci. Forum*, 1997, **239–241**, 573–576.

39 A. A. José, T. C. María and J. M. L. María, Preparation and topotactical oxidation of $ScVO_3$ with bixbyte structure: a low-temperature route to stabilize the new defect fluorite $ScVO_{3.5}$ metastable phase, *Dalton Trans.*, 2004, 1294–1297.

40 H. J. Cong, H. J. Zhang, B. Yao, W. T. Yu, X. Zhao, J. Y. Wang and G. C. Zhang, $ScVO_4$: Explorations of Novel Crystalline Inorganic Optical Materials in Rare-Earth Orthovanadate Systems, *Cryst. Growth Des.*, 2010, **10**, 4389–4400.

41 A. L. Joey, J. S. Fabian, S. W. Pamela, S. Kalpana, T. Venkataraman and B. Mario, Structure Evolution and Reactivity of the $Sc_{(2-x)}V_xO_{3+\delta}$ $(0 \leq x \leq 2.0)$ System, *Inorg. Chem.*, 2018, **57**, 5607–5614.

42 P. S. Shahid, J. L. Rylan, M. D. C. Lachlan and B. Mario, Formation, structure and magnetism of the metastable defect fluorite phases $AVO_{3.5+x}$ (A = In, Sc), *J. Solid State Chem.*, 2007, **180**, 3333–3340.

43 P. S. Shahid, W. K. Matthew, M. D. C. Lachlan, K. M. Vladimir, K. Scott and B. Mario, *In Situ* Powder X-ray Diffraction, Synthesis, and Magnetic Properties of the Defect Zircon Structure $ScVO_{4-x}$, *Inorg. Chem.*, 2009, **48**, 10553–10559.

44 F. W. Kang, Y. Zhang, L. Wondraczek, J. Q. Zhu, X. B. Yang and M. Y. Peng, Processing-dependence and the nature of the blue-shift of Bi^{3+}-related photoemission in $ScVO_4$ at elevated temperatures, *J. Mater. Chem. C*, 2014, **2**, 9850–9857.

45 H. S. Zhang, F. W. Kang, Y. J. Zhao, M. Y. Peng, D. Y. Lei and X. B. Yang, The role of oxygen defects in a bismuth doped $ScVO_4$ matrix: tuning luminescence by hydrogen treatment, *J. Mater. Chem. C*, 2017, **5**, 314–321.

46 G. Kresse and J. Hafner, *Ab initio* molecular dynamics for liquid metals, *Phys. Rev. B: Condens. Matter Mater. Phys.*, 1993, **47**, 558–561.

47 G. Kresse and D. Joubert, From ultrasoft pseudopotentials to the projector augmented-wave method, *Phys. Rev. B: Condens. Matter Mater. Phys.*, 1999, **59**, 1758–1775.

48 J. P. Perdew, K. Burke and M. Ernzerhof, Generalized Gradient Approximation Made Simple, *Phys. Rev. Lett.*, 1996, **77**, 3865–3868.

49 A. V. Krukau, O. A. Vydrov, A. F. Izmaylov and G. E. Scuseria, Influence of the Exchange Screening Parameter on the Performance of Screened Hybrid Functionals, *J. Chem. Phys.*, 2006, **125**, 224106.

50 J. C. Phillips, Dielectric Definition of Electronegativity, *Phys. Rev. Lett.*, 1968, **20**, 11–13.

51 J. A. Van Vechten, Quantum Dielectric Theory of Electronegativity in Covalent Systems. I. Electronic Dielectric Constant, *Phys. Rev.*, 1969, **182**, 891–905.

52 B. F. Levine, *d*-Electron Effects on Bond Susceptibilities and Ionicities, *Phys. Rev. B: Condens. Matter Mater. Phys.*, 1973, **7**, 2591–2600.

53 J. S. Shi, Z. J. Wu, S. H. Zhou and S. Y. Zhang, Dependence of crystal field splitting of 5d levels on hosts in the halide crystals, *Chem. Phys. Lett.*, 2003, **280**, 245–250.

54 J. S. Shi and S. Y. Zhang, Barycenter of Energy of Lanthanide $4f^{N-1}5d$ Configuration in Inorganic Crystals, *J. Phys. Chem. B*, 2004, **108**, 18845–18849.

55 Q. Su, J. Wang and J. S. Shi, Prediction and assignment of site occupation and energy levels for Pb^{2+} ions in crystal hosts, *J. Solid State Chem.*, 2010, **183**, 1174–1779.

56 L. Wang, Q. Su, Q. Liu and J. S. Shi, Investigation and application of quantitative relationship between sp energy levels of Bi^{3+} ion and host lattice, *J. Solid State Chem.*, 2012, **191**, 142–146.

57 M. Amer and P. Boutinaud, The doping sites in Eu^{2+}-doped $A^{I}B^{II}PO_4$ phosphors and their consequence on the photoluminescence excitation spectra, *J. Solid State Chem.*, 2018, **258**, 124–130.

58 K. Momma and F. Izumi, VESTA: a three-dimensional visualization system for electronic and structural analysis, *J. Appl. Crystallogr.*, 2008, **41**, 653–658.

59 N. E. Brese and M. O'Keefe, Bond-valence parameters for solids, *Acta Crystallogr.*, 1991, **B47**, 192–197.

60 J. Yang, J. W. Zhang, Z. Y. Gao, M. X. Tao, P. P. Dang, Y. Wei and G. G. Li, Enhanced photoluminescence and thermal stability in solid solution $Ca_{1-x}Sr_xSc_2O_4$:Ce^{3+} $(x = 0–1)$ *via* crystal field regulation and site-preferential occupation, *Inorg. Chem. Front.*, 2019, **6**, 2004–2013.

61 H. M. Li, R. Pang, G. Y. Liu, W. Z. Sun, D. Li, L. H. Jiang, S. Zhang, C. Y. Li, J. Feng and H. J. Zhang, Synthesis and Luminescence Properties of Bi^{3+}-Activated K_2MgGeO_4: A Promising High-Brightness Orange-Emitting Phosphor for WLEDs Conversion, *Inorg. Chem.*, 2018, **57**, 12303–12311.

62 T. Katsumata, H. Takashima, T. Michino and Y. Nobe, Non-stoichiometry in yttrium ortho-vanadate, *Mater. Res. Bull.*, 1994, **29**, 1247–1254.

63 N. Garces, K. Stevens, G. Foundos and L. Halliburton, Electron paramagnetic resonance and optical absorption study of V^{4+} centres in YVO_4, *J. Phys.: Condens. Matter*, 2004, **16**, 7095–7106.

64 A. L. Joey, M. S. Kevin, Z. S. Arzoo, R. W. Christopher and B. Mario, Order/Disorder and *in Situ* Oxide Defect Control in the Bixbyite Phase $YPrO_{3+\delta}$ $(0 \leq \delta < 0.5)$, *Inorg. Chem.*, 2016, **55**, 2381–2389.

65 L. Yang, G. Li, M. Zhao, J. Zheng, X. Guan and L. Li, Preparation and morphology sensitive luminescence properties of Eu^{3+}-doped YVO_4: a defect chemistry viewpoint of study, *CrystEngComm*, 2012, **14**, 3227–3235.

66 G. Blasse, The luminescence of closed-shell transition metal complexes. New developments, *Struct. Bonding*, 1980, **42**, 1–41.

67 C. M. Aiube, T. M. Lobo, D. Sousz-Moura, I. B. M. Ferraz, M. E. Osugi, C. K. Grisolia, R. Oliveira and I. T. Weber, Study of YVO_4 as a photocatalyst: correlation between synthetic route and ecotoxicity, *J. Environ. Chem. Eng.*, 2018, **6**, 2846–2854.

68 G. Boulon, Processus de photoluminescence dans les oxydes et les orthovanadates de terres rares polycristallins, activés par l'ion Bi^{3+}, *J. Phys.*, 1971, **32**, 333–347.

69 H. Ronde and G. Blasse, The nature of the electronic transition of the vanadate groups, *J. Inorg. Nucl. Chem.*, 1978, **40**, 215–219.

70 L. Yang, G. Li, W. Hu, M. Zhao, L. Sun and J. Zheng, Control over the crystallinity and defect chemistry of YVO_4

nanocrystals for optimum photocatalytic property, *Eur. J. Inorg. Chem.*, 2011, 2211–2220.

71 L. Qian, J. Zhu, Z. Chen, Y. Gui, Q. Gong and Y. Yuan, Self-assembled heavy lanthanide orthovanadate architecture with controlled dimensionality and morphology, *Chem. – Eur. J.*, 2009, **15**, 1233–1240.

72 Y. Nobe, H. Takashima and T. Katsumata, Decoloration of yttrium orthovanadate laser host crystals by annealing, *Opt. Lett.*, 1994, **19**, 1216–1218.

73 G. Blasse, Some considerations and experiments on concentration quenching of characteristic broad-band fluorescence, *Philips Res. Rep.*, 1968, **23**, 344.

74 W. Z. Lv, Y. C. Jia, Q. Zhao, M. M. Jiao, B. Q. Shao, W. Lü and H. P. You, Crystal Structure and Luminescence Properties of $Ca_8Mg_3Al_2Si_7O_{28}$:Eu^{2+} for WLEDs, *Adv. Opt. Mater.*, 2014, **2**, 183–188.

75 M. Janulevicius, P. Marmokas, M. Misevicius, J. Grigorjevaite, L. Mikoliunaite, S. Sakirzanovas and A. Katelnikovas, Luminescence and luminescence quenching of highly efficient $Y_2Mo_4O_{15}$:Eu^{3+} phosphors and ceramics, *Sci. Rep.*, 2016, **6**, 26098.

76 X. C. Wang, T. Seto, Z. Y. Zhao, Y. Y. Li, Q. S. Qu, H. Li and Y. S. Wang, Preparation of $Sr_{1-x}Ca_xYSi_4N_7$:Eu^{2+} solid solutions and their luminescence properties, *J. Mater. Chem. C*, 2014, **2**, 4476–4481.

77 G. Blasse and A. Bril, Photoluminescent efficiency of phosphors with electronic transitions in localized centers, *J. Electrochem. Soc.*, 1968, **115**, 1067–1075.

78 A. B. Garg, D. Errandonea, P. Rodriguez-Hernandez and A. Munoz, $ScVO_4$ under non-hydrostatic compression: a new metastable polymorph, *J. Phys.: Condens. Matter*, 2017, **29**, 055401.

79 M. Giarola, A. Sanson, A. Rahman, G. Mariotto, M. Bettinelli, A. Speghini and E. Cazzanelli, Virational dynamics of YPO_4 and $ScPO_4$ single crystals: an integrated study by polarized Raman spectroscopy and first-principles calculations, *Phys. Rev.*, 2011, **83**, 224302.

80 B. I. Won, B. Stuart, H. Jerry, M. Alexander, P. D. Steven and S. Ram, $Sr_{2.975-x}Ba_xCe_{0.025}AlO_4F$: a Highly Efficient Green-Emitting Oxyfluoride Phosphor for Solid State White Lighting, *Chem. Mater.*, 2010, **22**, 2842–2849.

81 F. W. Kang, Y. Zhang and M. Y. Peng, Controlling the Energy Transfer via Multi Luminescent Centers to Achieve White Light/Tunable Emissions in a Single-Phased X2-Type Y_2SiO_5:Eu^{3+},Bi^{3+} Phosphor For Ultraviolet Converted LEDs, *Inorg. Chem.*, 2015, **54**, 1462–1473.

82 F. W. Kang, G. H. Sun, P. Boutinaud, H. Y. Wu, F.-X. Ma, J. Lu, J. L. Gan, H. D. Bian, F. Gao and S. S. Xiao, Recent advances and prospects of persistent luminescent materials as inner secondary self-luminous light source for photocatalytic applications, *Chem. Eng. J.*, 2021, **403**, 126099.

83 P. P. Dang, D. J. Liu, Y. Wei, G. G. Li, H. Z. Lian, M. M. Shang and J. Lin, Highly Efficient Cyan-Green Emission in Self-Activated $Rb_3RV_2O_8$ (R = Y, Lu) Vanadate Phosphors for Full-Spectrum White Light-Emitting Diodes (LEDs), *Inorg. Chem.*, 2020, **59**, 6026–6038.

84 Y. L. Huang, Y. M. Yu, T. J. Tsuboi and H. J. Seo, Novel yellow-emitting phosphors of $Ca_5M_4(VO_4)_6$ (M = Mg, Zn) with isolated VO_4 tetrahedra, *Opt. Express*, 2012, **20**, 4360–4368.

85 J. C. Zhou, F. Huang, J. Xu, H. Chen and Y. S. Wang, Luminescence study of a self-activated and rare earth activated $Sr_3La(VO_4)_3$ phosphor potentially applicable in W-LEDs, *J. Mater. Chem. C*, 2015, **3**, 3023–3028.

86 R. J. Yu, M. S. Yuan, T. B. Li, Q. Tu and J. Y. Wang, Preparation, structure and luminescence properties of $Ba_2V_2O_7$ microrods, *RSC Adv.*, 2016, **6**, 90711–90717.

87 T. Nakajima, M. Isobe, T. Tsuchiya, Y. Ueda and T. Manabe, Photoluminescence property of vanadates $M_2V_2O_7$ (M: Ba, Sr and Ca), *Opt. Mater.*, 2010, **32**, 1618–1621.

88 T. Nakajima, M. Isobe, T. Tsuchiya, Y. Ueda and T. Manabe, Correlation between Luminescence Quantum Efficiency and Structural Properties of Vanadate Phosphors with Chained, Dimerized, and Isolated VO_4 Tetrahedra, *J. Phys. Chem. C*, 2010, **114**, 5160–5167.

89 X. Y. Huang, S. Y. Wang, S. Rtimi and B. Devakumar, $KCa_2Mg_2V_3O_{12}$: a novel efficient rare-earth-free self-activated yellow-emitting phosphor, *J. Photochem. Photobiol., A*, 2020, **401**, 112765.

90 W. Zheng, P. Huang, Z. L. Gong, D. D. Tu, J. Xu, Q. L. Zou, R. F. Li, W. W. You, J. C. G. Bünzli and X. Y. Chen, Near-infrared-triggered photon upconversion tuning in all-inorganic cesium lead halide perovskite quantum dots, *Nat. Commun.*, 2018, **9**, 3462.

91 Y. N. Liu, G. C. Pan, R. Wang, H. Shao, H. Wang, W. Xu, H. N. Cui and H. W. Song, Considerably enhanced exciton emission of $CsPbCl_3$ perovskite quantum dots by the introduction of potassium and lanthanide ions, *Nanoscale*, 2018, **10**, 14067–14072.

92 W. Y. Liu, Q. L. Lin, H. B. Li, K. F. Wu, I. Robel, J. M. Pietryga and V. I. Klimov, Mn^{2+}-Doped Lead Halide Perovskite Nanocrystals with Dual-Color Emission Controlled by Halide Content, *J. Am. Chem. Soc.*, 2016, **138**, 14954–14961.

93 L. Q. Mi, Y. L. Huang, L. Cao, Y. Y. Feng and H. J. Seo, Modified optical properties via induced cation disorder in self-activated $NaMg_2V_3O_{10}$, *Dalton Trans.*, 2018, **47**, 4368–4376.

94 L. K. Bharat, S.-K. Jeon, K. G. Krishna and J. S. Yu, Rare-earth free self-luminescent $Ca_2KZn_2(VO_4)_3$ phosphors for intense white light-emitting diodes, *Sci. Rep.*, 2017, **7**, 42348.

95 E. Pavitra, G. S. R. Raju, L. K. Bharat, J. Y. Park, C. H. Kwak, J. W. Chun, Y.-K. Han and Y. S. Huh, Evolution of highly efficient rare-earth free $Cs_{(1-x)}Rb_xVO_3$ phosphors as a single emitting component for NUV-based white LEDs, *J. Mater. Chem. C*, 2018, **6**, 12746–12757.

